



Nonlinear waves in a strongly nonlinear resonant granular chain

Lifeng Liu, Guillaume James, Panayotis Kevrekidis, Anna Vainchtein

► To cite this version:

Lifeng Liu, Guillaume James, Panayotis Kevrekidis, Anna Vainchtein. Nonlinear waves in a strongly nonlinear resonant granular chain. 2015. hal-01161719

HAL Id: hal-01161719

<https://hal.science/hal-01161719>

Preprint submitted on 9 Jun 2015

HAL is a multi-disciplinary open access archive for the deposit and dissemination of scientific research documents, whether they are published or not. The documents may come from teaching and research institutions in France or abroad, or from public or private research centers.

L'archive ouverte pluridisciplinaire **HAL**, est destinée au dépôt et à la diffusion de documents scientifiques de niveau recherche, publiés ou non, émanant des établissements d'enseignement et de recherche français ou étrangers, des laboratoires publics ou privés.

Nonlinear waves in a strongly nonlinear resonant granular chain

Lifeng Liu¹, Guillaume James², Panayotis Kevrekidis^{3,4}, and Anna Vainchtein¹

¹*Department of Mathematics, University of Pittsburgh, Pittsburgh, Pennsylvania 15260, USA*

²*INRIA Grenoble - Rhône-Alpes, Bipop Team-Project, Inovallée, 655 Avenue de l'Europe, 38334 Saint Ismier Cedex, France.*

³*Department of Mathematics and Statistics, University of Massachusetts, Amherst, Massachusetts 01003, USA*

⁴*Theoretical Division and Center for Nonlinear Studies, Los Alamos National Laboratory, Los Alamos, New Mexico 87545, USA*

June 9, 2015

Abstract

We explore a recently proposed locally resonant granular system bearing harmonic internal resonators in a chain of beads interacting via Hertzian elastic contacts. In this system, we propose the existence of two types of configurations: (a) small-amplitude periodic traveling waves and (b) dark-breather solutions, i.e., exponentially localized, time periodic states mounted on top of a non-vanishing background. We also identify conditions under which the system admits long-lived bright breather solutions. Our results are obtained by means of an asymptotic reduction to a suitably modified version of the so-called discrete p-Schrödinger (DpS) equation, which is established as controllably approximating the solutions of the original system for large but finite times (under suitable assumptions on the solution amplitude and the resonator mass). The findings are also corroborated by detailed numerical computations. A remarkable feature distinguishing our results from other settings where dark breathers are observed is the complete *absence* of precompression in the system, i.e., the absence of a linear spectral band.

1 Introduction

Granular materials, tightly packed aggregates of particles that deform elastically when in contact with each other, provide a natural setting for the study of nonlinear waves. Under certain assumptions, dynamics of granular crystals is governed by Hertzian contact interactions of the particles [1–3]. This leads to the emergence of a wide variety of nonlinear

waves. Among them, arguably, the most prototypical ones are traveling waves [1–3], shock waves [4, 5] and exponentially localized (in space), periodic (in time) states that are referred to as discrete breathers [6–8].

Discrete breathers constitute a generic excitation that emerges in a wide variety of systems and has been thoroughly reviewed [9, 10]. Discrete breathers can be divided into two distinct types, which are often referred to as *bright* and *dark* breathers. Bright breathers have tails in relative displacement decaying to zero and are known to exist in dimer (or more generally heterogeneous) granular chains with precompression [6, 11, 12], monatomic granular chains with defects [13] (see also [14]) and in Hertzian chains with harmonic onsite potential [15–17]. Dark breathers are spatially modulated standing waves whose amplitude is constant at infinity and vanishes at the center of the chain (see Fig. 9, for example). Their existence, stability and bifurcation structures have been studied in a homogeneous granular chain under precompression [18]. Recently, experimental investigations utilizing laser Doppler vibrometry have systematically revealed the existence of such states in damped, driven granular chains in [7]. However, to the best of our knowledge, dark breathers have *not* been identified in a monatomic granular chain without precompression.

In this work, we focus on a recent, yet already emerging as particularly interesting, modification of the standard granular chain, namely the so-called locally resonant granular chain. The latter belongs to a new type of granular “metamaterial” that has additional degrees of freedom and exhibits a very rich nonlinear dynamic behavior. In particular, in these systems it is possible to engineer tunable band gaps, as well as to potentially utilize them for shock absorption and vibration mitigation. Such metamaterials have been recently designed and experimentally tested in the form of chains of spherical beads with internal linear resonators inside the primary beads (mass-in-mass chain) [19], granular chains with external ring resonators attached to the beads (mass-with-mass chain) [20] (see also [21]) and woodpile phononic crystals consisting of vertically stacked slender cylindrical rods in orthogonal contact [22]. An intriguing feature that has already been reported in such systems is the presence of weakly nonlinear solitary waves or nanoptera [23] (see also [24] for more detailed numerical results). Under certain conditions, each of these systems can be described by a granular chain with a secondary mass attached to each bead in the chain by a linear spring. The attached linear oscillator has the natural frequency of the internal resonator in the mass-in-mass chain (Fig. 1 in [19]), the piston normal vibration mode of the ring resonator attached to each bead in the mass-with-mass system (Fig. 9 in [20]) or the primary bending vibration mode of the cylindrical rods in the woodpile setup (Fig. 1 in [22]).

One of the particularly appealing characteristics of a locally resonant granular chain of this type is the fact that it possesses a number of special case limits that have previously been studied. More specifically, in the limit when the ratio of secondary to primary masses tends to zero, our model reduces to the non-resonant, homogeneous granular chain, while at a very large mass ratio and zero initial conditions for the secondary mass the system approaches a model of Newton’s cradle [15], a granular chain with quadratic onsite potential. In [15] (see also [16, 17, 25]), the so-called discrete p-Schrödinger (DpS) modulation equation governing slowly varying small amplitude of oscillations was derived and used to prove existence of (and numerically compute) time-periodic traveling wave solutions and study other periodic solutions such as standing and traveling breathers.

In the present setting of locally resonant granular crystals, we explore predominantly two

classes of solutions, namely (a) small-amplitude periodic traveling waves and (b) (dark) discrete breathers. To investigate these solutions at finite mass ratio (i.e., away from the above studied limits), we follow a similar approach and derive generalized modulation equations of the DpS type. We show that these equations capture small-amplitude periodic traveling waves of the system quite well when the mass ratio is below a critical value. We observe that the system admits only trivial exact bright breathers that involve linear oscillations. However, we use the DpS framework to prove that when the mass ratio is sufficiently large, the system has *long-lived* nontrivial bright breathers for suitable initial conditions. We also use solutions of the DpS equations to form initial conditions for numerical computation of dark breather solutions, whose stability and bifurcation structure are examined for different mass ratios. When the breather frequency is above the linear frequency of the resonator but sufficiently close to it, we identify two families of dark breathers, as is often the case in nonlinear lattice dynamical systems [10]. The dark breather solutions of site-centered type are long-lived and exhibit marginal oscillatory instability. Meanwhile, the bond-centered solutions exhibit real instability. This can lead to the emergence of steadily traveling dark breathers in the numerical simulations. In addition, we identify period-doubling bifurcations for the bond-centered solutions. The instability of breather solutions is also affected by the mass ratio. In particular, the real instability of the bond-centered breather solutions at a given frequency gradually becomes stronger as the mass ratio increases.

The paper is organized as follows. Sec. 2 introduces the model, and the generalized DpS equations are derived in Sec. 3.1. In Sec. 3.2 we show that for sufficiently large mass ratio the equations reduce to the DpS equation derived in [15] and rigorously justify the validity of this equation on the long-time scale for suitable small-amplitude initial data. We use the modulation equations in Sec. 4 to numerically investigate small-amplitude time-periodic traveling waves, including their stability, the accuracy of their DpS approximation and the effect of the mass ratio. In Sec. 5 we show that the system admits only trivial exact bright breather solutions that do not involve Hertzian interactions. We then prove and numerically demonstrate the existence of long-lived nontrivial bright breathers at sufficiently large mass ratio. In Sec. 6 we construct the approximate dark breather solutions using the DpS equations. We use these solutions and a continuation procedure based on Newton-type method to compute numerically exact dark breathers and examine their stability and bifurcation structure in Sec. 7. Concluding remarks can be found in Sec. 8.

2 The model

Consider a chain of identical particles of mass m_1 and suppose a secondary particle of mass m_2 is attached to each primary one via a linear spring of stiffness $K > 0$ and constrained to move in the horizontal direction. As mentioned in the Introduction, the harmonic oscillator is meant to represent the primary vibration mode of a ring resonator attached to each primary mass or a cylindrical rod. Let $\tilde{u}_n(\tilde{t})$ and $\tilde{v}_n(\tilde{t})$ denote the displacements of the n th primary and secondary masses, respectively. The dynamics of the resulting locally resonant granular

chain is governed by

$$\begin{aligned} m_1 \frac{d^2 \tilde{u}_n}{dt^2} &= \mathcal{A}(\tilde{u}_{n-1} - \tilde{u}_n)_+^\alpha - \mathcal{A}(\tilde{u}_n - \tilde{u}_{n+1})_+^\alpha - K(\tilde{u}_n - \tilde{v}_n), \\ m_2 \frac{d^2 \tilde{v}_n}{dt^2} &= K(\tilde{u}_n - \tilde{v}_n). \end{aligned} \quad (1)$$

Here $\mathcal{A}(\tilde{u}_n - \tilde{u}_{n+1})_+^\alpha$ is the Hertzian contact interaction force between n th and $(n+1)$ th particles, where $(x)_+ = x$ when $x > 0$ and equals zero otherwise, so the particles interact only when they are in contact, $\mathcal{A} > 0$ is the Hertzian constant, which depends on the material properties of the contacting particles and radius of the contact curvature, and α is the nonlinear exponent of the contact interaction that depends on the shape of the particles and the mode of contact (e.g. $\alpha = 3/2$ for spherical beads and orthogonally stacked cylinders). Typically, we find $\alpha > 1$, although settings with $\alpha < 1$ have also been proposed; see e.g. [26] and references therein. In writing (1) we assume that the deformation of the particles in contact is confined to a sufficiently small region near the contact point and varies slowly enough on the time scale of interest, so that the static Hertzian law still holds [3]; this is known to be a well justified approximation in a variety of different settings [1, 2]. We also assume that dissipation and plastic deformation are negligible, which is generally a reasonable approximation, although dissipation effects have been argued to potentially lead to intriguing features in their own right, including secondary waves [27] (see also [28]). Choosing R to be a characteristic length scale, for example, the radius of spherical or cylindrical particles, we can introduce dimensionless variables

$$u_n = \frac{\tilde{u}_n}{R}, \quad v_n = \frac{\tilde{v}_n}{R}, \quad t = \tilde{t} \sqrt{\frac{R^{\alpha-1} \mathcal{A}}{m_1}}$$

and two dimensionless parameters

$$\rho = \frac{m_2}{m_1}, \quad \kappa = \frac{K}{\mathcal{A} R^{\alpha-1}},$$

where ρ is the ratio of two masses and κ measures the relative strength of the linear elastic spring. In the dimensionless variables the equations (1) become

$$\begin{aligned} \ddot{u}_n &= (u_{n-1} - u_n)_+^\alpha - (u_n - u_{n+1})_+^\alpha - \kappa(u_n - v_n) \\ \rho \ddot{v}_n &= \kappa(u_n - v_n), \end{aligned} \quad (2)$$

where \ddot{u}_n and \ddot{v}_n are second time derivatives. In what follows, it will be sometimes convenient to consider (2) rewritten in terms of relative displacement (strain) variables $x_n = u_n - u_{n-1}$ and $y_n = v_n - v_{n-1}$:

$$\begin{aligned} \ddot{x}_n &= 2(-x_n)_+^\alpha - (-x_{n+1})_+^\alpha - (-x_{n-1})_+^\alpha - \kappa(x_n - y_n) \\ \rho \ddot{y}_n &= \kappa(x_n - y_n). \end{aligned} \quad (3)$$

Note that in the limit $\rho \rightarrow 0$, the model reduces to the one for a regular (non-resonant) homogeneous granular chain. Meanwhile, at $\rho \rightarrow \infty$ and zero initial conditions for $v_n(t)$

the system approaches a model of Newton's cradle, a granular chain with quadratic onsite potential, which is governed by [15, 29]

$$\ddot{u}_n + \kappa u_n = (u_{n-1} - u_n)_+^\alpha - (u_n - u_{n+1})_+^\alpha. \quad (4)$$

In [15], the discrete p-Schrödinger (DpS) equation

$$2i\tau_0 \frac{\partial A_n}{\partial \tau} = (A_{n+1} - A_n)|A_{n+1} - A_n|^{\alpha-1} - (A_n - A_{n-1})|A_n - A_{n-1}|^{\alpha-1} \quad (5)$$

has been derived at $\kappa = 1$ to capture the modulation of small-amplitude nearly harmonic oscillations in the form

$$u_n^{app}(t) = \varepsilon(A_n(\tau)e^{it} + \bar{A}_n(\tau)e^{-it}), \quad \tau = \varepsilon^{\alpha-1}t, \quad (6)$$

where $\varepsilon > 0$ is a small parameter, $A_n(\tau)$ is a slowly varying amplitude of the oscillations and τ_0 is a constant depending on α . In the next section, we follow a similar approach and use multiscale expansion to derive generalized modulation equations of the DpS type for (2) with finite ρ .

3 Modulation equations for small amplitude waves

3.1 Derivation of generalized DpS equations at finite ρ

Using the two-timing asymptotic expansion as in [15], we seek solutions of (2) in the form

$$u(t) = \varepsilon U(t, \tau), \quad v(t) = \varepsilon V(t, \tau)$$

where $\tau = \varepsilon^{\alpha-1}t$ is the slow time, and u, v, U and V are vectors with components u_n, v_n, U_n, V_n , respectively. The governing equations (2) then yield

$$\begin{aligned} (\partial_t + \varepsilon^{\alpha-1}\partial_\tau)^2 U &= \varepsilon^{\alpha-1}G(U) + \kappa(V - U) \\ (\partial_t + \varepsilon^{\alpha-1}\partial_\tau)^2 V &= \frac{\kappa}{\rho}(U - V), \end{aligned} \quad (7)$$

where the nonlinear term is given by

$$G(U)_n = (U_{n-1} - U_n)_+^\alpha - (U_n - U_{n+1})_+^\alpha.$$

The solution has the form

$$U = U^0 + \varepsilon^{\alpha-1}U^1 + o(\varepsilon^{\alpha-1}), \quad V = V^0 + \varepsilon^{\alpha-1}V^1 + o(\varepsilon^{\alpha-1}).$$

The 0th order terms satisfy a linear system, which after the elimination of secular terms yields

$$U^0 = B(\tau) + \kappa[A(\tau)e^{i\omega t} + \bar{A}(\tau)e^{-i\omega t}], \quad V^0 = B(\tau) - \frac{\kappa}{\rho}[A(\tau)e^{i\omega t} + \bar{A}(\tau)e^{-i\omega t}], \quad (8)$$

where $\omega = \sqrt{\kappa + \kappa/\rho}$ is the frequency of harmonic oscillations. This internal frequency of each resonator is associated with the out-of-phase motion of the displacements U and V . On the order $O(\varepsilon^{\alpha-1})$, the system (7) results in

$$\begin{aligned} (\partial_t^2 + \kappa)U^1 - \kappa V^1 &= -2\kappa\partial_\tau A i\omega e^{i\omega t} + c.c. + G(U^0) \\ \partial_t^2 V^1 - \frac{\kappa}{\rho}(U^1 - V^1) &= \frac{2\kappa}{\rho}\partial_\tau A i\omega e^{i\omega t} + c.c., \end{aligned} \quad (9)$$

where $c.c.$ denotes the complex conjugate. Let

$$J(f) = \frac{\omega}{2\pi} \int_0^{2\pi/\omega} f(t) e^{-i\omega t} dt \quad (10)$$

denote the projection of $f(t)$ on $e^{i\omega t}$ and define the averaging operator as

$$E(f) = \frac{\omega}{2\pi} \int_0^{2\pi/\omega} f(t) dt. \quad (11)$$

The projection operator on all remaining Fourier modes (of the form $e^{ij\omega t}$, $j \neq \pm 1$, $j \neq 0$) is given by

$$\Pi_h = I - E - e^{i\omega t} J - e^{-i\omega t} \bar{J}. \quad (12)$$

Let $U_h^1 = \Pi_h U^1$, $V_h^1 = \Pi_h V^1$. Then (9) yields

$$\begin{aligned} (\partial_t^2 + \kappa)U_h^1 - \kappa V_h^1 &= \Pi_h G(U^0) \\ \partial_t^2 V_h^1 - \frac{\kappa}{\rho}(U_h^1 - V_h^1) &= 0. \end{aligned}$$

Note that this equation has a unique $2\pi/\omega$ -periodic solution $(U_h^1, V_h^1)^T$ because for each j such that $j \neq \pm 1$, $j \neq 0$, the matrix

$$\begin{bmatrix} \kappa - j^2\omega^2 & -\kappa \\ -\kappa/\rho & \kappa/\rho - j^2\omega^2 \end{bmatrix}$$

for the left hand side of the above equation associated with j th harmonic is invertible. Let

$$U^1 = U_h^1 + C^0(\tau) + C^1(\tau)e^{i\omega t} + c.c., \quad V^1 = V_h^1 + D^0(\tau) + D^1(\tau)e^{i\omega t} + c.c.$$

and project (9) on $e^{i\omega t}$, recalling that $\omega = \sqrt{\kappa + \kappa/\rho}$:

$$\begin{aligned} -(\kappa/\rho)C^1 - \kappa D^1 &= -2\kappa\partial_\tau A i\omega + J(G(U^0)) \\ -(\kappa/\rho)C^1 - \kappa D^1 &= (2\kappa/\rho)\partial_\tau A i\omega. \end{aligned}$$

This yields the compatibility condition

$$2i\kappa\omega^3\partial_\tau A = J(G(U^0)) \quad (13)$$

and

$$D^1 = -\frac{\kappa}{\rho}(C^1 + 2i\omega\partial_\tau A).$$

Taking the average of (9), we obtain

$$\begin{aligned}\kappa(C^0 - D^0) &= E(G(U^0)) \\ -\frac{\kappa}{\rho}(C^0 - D^0) &= 0.\end{aligned}$$

Since ρ is finite, this yields $C^0 = D^0$, and hence the following condition can be obtained for the leading order solution:

$$E(G(U^0)) = 0. \quad (14)$$

To obtain the generalized DpS equations, we now consider the conditions (13) and (14) in more detail. Observe that for $b \in \mathbb{R}$, $z = re^{i\theta} \in \mathbb{C}$, we have

$$E[(-b + \kappa z e^{i\omega t} + \kappa \bar{z} e^{-i\omega t})_+^\alpha] = \frac{1}{2\pi} \int_0^{2\pi} (-b + 2\kappa r \cos t)_+^\alpha dt \equiv g_\alpha(b, r), \quad r = |z|. \quad (15)$$

Here we rescaled time in the averaging integral and used the fact that the result is independent of θ since we can always shift time when averaging. Similarly,

$$J[(-b + \kappa z e^{i\omega t} + \kappa \bar{z} e^{-i\omega t})_+^\alpha] = \frac{z}{2\pi r} \int_0^{2\pi} e^{-it} (-b + 2\kappa r \cos t)_+^\alpha dt \equiv z h_\alpha(b, r), \quad r = |z|. \quad (16)$$

Defining the forward and backward shift operators

$$(\delta^+ A)_n = A_{n+1} - A_n, \quad (\delta^- A)_n = A_n - A_{n-1},$$

we observe that

$$G(U^0) = -\delta^+(-\delta^- U^0)_+^\alpha = -\delta^+(-\delta^- B(\tau) - \kappa \delta^- A(\tau) e^{i\omega t} - \kappa \delta^- \bar{A}(\tau) e^{-i\omega t})_+^\alpha,$$

where we used the first of (8) to obtain the second equality. Substituting this in (13) and (14) and using (15), (16) with $z = -\delta^- A$ and $b = \delta^- B$, we obtain the *generalized DpS equations*

$$2i\kappa\omega^3 \partial_\tau A = \delta^+[h_\alpha(\delta^- B, |\delta^- A|) \delta^- A] \quad (17)$$

and

$$\delta^+ g_\alpha(\delta^- B, |\delta^- A|) = 0. \quad (18)$$

3.2 DpS equation at large ρ

We now investigate the case of large ρ . Consider first the “critical” case when $\rho = \varepsilon^{1-\alpha}$. The 0th order problem is

$$\partial_t^2 U^0 = \kappa(V^0 - U^0), \quad \partial_t^2 V^0 = 0,$$

which yields

$$U^0 = B(\tau) + \kappa[A(\tau)e^{i\sqrt{\kappa}t} + \bar{A}(\tau)e^{-i\sqrt{\kappa}t}], \quad V^0 = B(\tau), \quad (19)$$

where we used the fact that $\omega = \sqrt{\kappa}$ when $\rho \rightarrow \infty$. Meanwhile, the $O(\varepsilon^{\alpha-1})$ problem becomes

$$\begin{aligned}(\partial_t^2 + \kappa)U^1 - \kappa V^1 &= -2i\kappa^{3/2} \partial_\tau A e^{i\sqrt{\kappa}t} + c.c. + G(U^0) \\ \partial_t^2 V^1 &= \kappa^2 A e^{i\sqrt{\kappa}t} + c.c.\end{aligned}$$

Note that the right hand side of the second equation has zero time average, as it should to be consistent with the left hand side, and the equation yields

$$V^1 = -\kappa A(\tau)e^{i\sqrt{\kappa}t} + c.c. + D^0(\tau).$$

Putting this back into the first equation and projecting on $e^{i\sqrt{\kappa}t}$, we get

$$2\kappa^{3/2}i\partial_\tau A + \kappa^2 A = J[G(U^0)],$$

which is *almost* like the DpS equation in [15] if we set $\kappa = 1$. Note, however, the additional term $\kappa^2 A$ in the left hand side and the fact that U^0 also includes $B(\tau)$. Observe further that there are no conditions to determine B at this order. If $B = 0$, we get a (modified) DpS equation for A only.

Now suppose $\rho = \varepsilon^{1-\gamma}$, $\gamma > \alpha$. Then the 0th order equation is the same, so the solution is still given by (19), while on $O(\varepsilon^{\alpha-1})$ we get

$$\begin{aligned} (\partial_t^2 + \kappa)U^1 - \kappa V^1 &= -2\kappa^{3/2}\partial_\tau A i e^{i\sqrt{\kappa}t} + c.c. + G(U^0) \\ \partial_t^2 V^1 &= 0, \end{aligned}$$

so the second equation yields $V^1 = D_0(\tau)$, while the projection of the first on $e^{i\sqrt{\kappa}t}$ yields the DpS equation for the Newton's cradle model:

$$2\kappa^{3/2}i\partial_\tau A = J[G(U^0)].$$

Note that $B(\tau)$ in (19) is again not determined at this order. Observe, however, that in the limit $\rho \rightarrow \infty$ the initial conditions $v(0) = \dot{v}(0) = 0$ yield $v(t) \equiv 0$ (and thus $V^0 = V^1 = 0$), and we recover (6) and the DpS equation (5) at $\kappa = 1$:

$$i\partial_\tau A = \omega_0 \delta^+ [|\delta^- A|^{\alpha-1} \delta^- A] \quad (20)$$

with (see [15])

$$\omega_0 = \frac{2^{\alpha-2}}{\sqrt{\pi}} \frac{\Gamma(\alpha/2 + 1)}{\Gamma((\alpha + 1)/2 + 1)}. \quad (21)$$

In Theorem 3.1 below, we justify the DpS equation (20) on long time scales, for suitable small-amplitude initial conditions. We obtain error estimates between solutions of (2) and modulated profiles described by DpS. We seek solutions of (2) and the DpS equation in the usual sequence spaces ℓ_p with $1 \leq p \leq +\infty$. For simplicity we state Theorem 3.1 in the case $\kappa = 1$.

Theorem 3.1 *Fix constants $C_r, C_i, T > 0$ and a solution $A \in \mathcal{C}^2([0, T], \ell_p)$ of the DpS equation (20). There exist constants $\varepsilon_T > 0$ and $C_T \geq C_i$ such that the following holds: For all $\varepsilon \leq \varepsilon_T$ and for $\rho^{-1} \leq C_r \varepsilon^{2(\alpha-1)}$, for all initial condition $(u(0), v(0), \dot{u}(0), \dot{v}(0)) \in \ell_p^4$ satisfying*

$$\|u(0) - 2\varepsilon \operatorname{Re} A(0)\|_p + \|\dot{u}(0) + 2\varepsilon \operatorname{Im} A(0)\|_p \leq C_i \varepsilon^\alpha, \quad (22)$$

$$\|v(0)\|_p \leq C_i \varepsilon^\alpha, \quad \|\dot{v}(0)\|_p \leq C_i \varepsilon^{2\alpha-1}, \quad (23)$$

the corresponding solution of (2) satisfies for all $t \in [0, T/\varepsilon^{\alpha-1}]$

$$\|u(t) - 2\varepsilon \operatorname{Re} (A(\varepsilon^{\alpha-1}t) e^{it})\|_p + \|\dot{u}(t) + 2\varepsilon \operatorname{Im} (A(\varepsilon^{\alpha-1}t) e^{it})\|_p \leq C_T \varepsilon^\alpha, \quad (24)$$

$$\|v(t)\|_p \leq C_T \varepsilon^\alpha, \quad \|\dot{v}(t)\|_p \leq C_T \varepsilon^{2\alpha-1}. \quad (25)$$

Similarly to what was established in [17] for Newton's cradle problem, Theorem 3.1 shows that small $O(\varepsilon)$ solutions of (2) are described by the DpS equation over long (but finite) times of order $\varepsilon^{1-\alpha}$. However, there are important differences compared to the results of [17]. Firstly, the DpS approximation is not valid for all small-amplitude initial conditions, since one has to assume that $v(0)$ and $\dot{v}(0)$ are small enough (see (23)). Secondly, ρ must be large when ε is small. More precisely, ρ must be greater than $\varepsilon^{2(1-\alpha)}$, which scales as the square of the characteristic time scale of DpS. This is due to the translational invariance of (2), which introduces a Jordan block in the linearization of (2) around the trivial state, inducing a quadratic growth of secular terms (see the estimate (44) below).

Let us now prove Theorem 3.1. The main steps are Gronwall estimates to obtain solutions of (2) close to solutions of the Newton's cradle problem (4) when ρ is large, and the use of the results of [17] to approximate solutions of (4) with the DpS equation.

Equation (2) at $\kappa = 1$ reads

$$\ddot{u} + u - v = G(u), \quad (26)$$

$$\ddot{v} = \sigma(u - v), \quad (27)$$

where $\sigma = 1/\rho$ is a small parameter satisfying

$$\sigma \leq C_r \varepsilon^{2(\alpha-1)}, \quad (28)$$

as assumed in Theorem 3.1. In addition, we have

$$\|G(u)\|_p = O(\|u\|_p^\alpha), \quad \|DG(u)\|_{\mathcal{L}(\ell_p)} = O(\|u\|_p^{\alpha-1}). \quad (29)$$

To simplify subsequent estimates, it is convenient to uncouple the linear parts of (26) and (27), which can be achieved by making the change of variables

$$u = Q + R, \quad v = R - \sigma Q.$$

The system (26)-(27) is equivalent to

$$\ddot{Q} + Q = \chi G(Q + R) - \sigma Q, \quad (30)$$

$$\ddot{R} = \chi \sigma G(Q + R), \quad (31)$$

where $\chi = (1 + \sigma)^{-1}$ is close to unity.

To approximate the dynamics of (30)-(31) when σ is small, we first consider the case $\sigma = 0$ and $R = 0$ of (30) (leading to the Newton's cradle problem) and use the results of [17] relating Newton's cradle problem to the DpS equation. More precisely, given the solution A of the DpS equation considered in Theorem 3.1, we introduce the solution Q_a of

$$\ddot{Q}_a + Q_a = G(Q_a)$$

with initial condition $Q_a(0) = 2\varepsilon \operatorname{Re} A(0)$, $\dot{Q}_a(0) = -2\varepsilon \operatorname{Im} A(0)$. According to Theorem 2.10 of [17], for ε small enough, the solution Q_a is defined on a maximal interval of existence (t^-, t^+) containing $[0, T \varepsilon^{1-\alpha}]$ and satisfies for all $t \in [0, T \varepsilon^{1-\alpha}]$

$$\|Q_a(t) - 2\varepsilon \operatorname{Re}(A(\varepsilon^{\alpha-1}t) e^{it})\|_p + \|\dot{Q}_a(t) + 2\varepsilon \operatorname{Im}(A(\varepsilon^{\alpha-1}t) e^{it})\|_p \leq C \varepsilon^\alpha. \quad (32)$$

This implies in particular that

$$\|Q_a\|_{L^\infty((0, T\varepsilon^{1-\alpha}), \ell_p)} + \|\dot{Q}_a\|_{L^\infty((0, T\varepsilon^{1-\alpha}), \ell_p)} \leq M\varepsilon. \quad (33)$$

Next, our aim is to show that Q remains close to Q_a (and its DpS approximation) and R remains small over long times, for suitable initial conditions, ε small enough and ρ large enough (i.e. σ small enough). Setting $Q = Q_a + W$ in (30)-(31) yields

$$\ddot{W} + W = N(W, R) \quad (34)$$

$$\ddot{R} = \chi\sigma G(Q_a + W + R), \quad (35)$$

where

$$N(W, R) = -\sigma(Q_a + \chi G(Q_a)) + \chi[G(Q_a + W + R) - G(Q_a)] - \sigma W. \quad (36)$$

Moreover, from the identities

$$W = Q - Q_a = (1 + \sigma)^{-1}(u - v) - Q_a, \quad R = (1 + \sigma)^{-1}(\sigma u + v)$$

and the assumptions (22)-(23) and (28), it follows that

$$\|W(0)\|_p + \|\dot{W}(0)\|_p \leq C\varepsilon^\alpha, \quad (37)$$

$$\|R(0)\|_p \leq C\varepsilon^\alpha, \quad \|\dot{R}(0)\|_p \leq C\varepsilon^{2\alpha-1}. \quad (38)$$

Let $X = (W, R, \dot{W}, \dot{R})$ and $\|X\|_p$ denote the sum of the ℓ_p norms of each component. We shall now use Gronwall estimates to bound $\|X(t)\|_p$ on the time scale considered in Theorem 3.1.

The solutions of (34)-(35) corresponding to initial conditions satisfying (37)-(38) are defined on a maximal interval of existence (t_{\min}, t_{\max}) with $t_{\min} < 0$ and $t_{\max} \leq t^+$, which depends a priori on the initial condition and parameters (in particular, ε). From (37)-(38), one can infer that $\|X(0)\|_p < M\varepsilon$ (the size of Q_a in (33)) for ε small enough. Let

$$t_\varepsilon = \sup \{t \in (0, \min(T\varepsilon^{1-\alpha}, t_{\max})) : \forall s \in (0, t), \|X(s)\|_p \leq M\varepsilon\}. \quad (39)$$

From (33) and the triangle inequality, we obtain

$$\|Q_a(t) + W(t) + R(t)\|_p \leq 2M\varepsilon, \quad \forall t \in [0, t_\varepsilon]. \quad (40)$$

In addition, from definition (39) we have either

$$t_\varepsilon < \min(T\varepsilon^{1-\alpha}, t_{\max}) \text{ and } \|X(t_\varepsilon)\|_p = M\varepsilon \quad (41)$$

or

$$t_\varepsilon = T\varepsilon^{1-\alpha} < t_{\max} \quad (42)$$

(if $\|X\|_p$ is bounded on $[0, t_{\max})$, then $t_{\max} = t^+ > T\varepsilon^{1-\alpha}$). Integrating (35) twice yields

$$R(t) = \dot{r}(0)t + R(0) + \chi\sigma \int_0^t (t-s) G(Q_a + W + R)(s) ds. \quad (43)$$

Using the fact that $t_\varepsilon \leq T \varepsilon^{1-\alpha}$, estimate (40) and the first bound in (29), one obtains from the above identity the following inequality:

$$\forall t \in [0, t_\varepsilon], \|R(t)\|_p \leq T \varepsilon^{1-\alpha} \|\dot{R}(0)\|_p + \|R(0)\|_p + C_1 \sigma \varepsilon^{2-\alpha}. \quad (44)$$

Then the assumption (28) and the property (38) yield

$$\forall t \in [0, t_\varepsilon], \|R(t)\|_p \leq C \varepsilon^\alpha. \quad (45)$$

Similarly, we have

$$\dot{R}(t) = \dot{R}(0) + \chi \sigma \int_0^t G(Q_a + W + R)(s) ds, \quad (46)$$

which implies

$$\forall t \in [0, t_\varepsilon], \|\dot{R}(t)\|_p \leq \|\dot{R}(0)\|_p + O(\sigma \varepsilon) \leq C \varepsilon^{2\alpha-1}. \quad (47)$$

Moreover, using Duhamel's formula in (34) yields

$$W(t) = \cos t W(0) + \sin t \dot{W}(0) + \int_0^t \sin(t-s) [N(W, R)](s) ds.$$

Recalling that $t_\varepsilon \leq T \varepsilon^{1-\alpha}$, using (37), and using (33), (28), (29) and (45) to estimate $N(W, R)$ from the definition (36), we get

$$\forall t \in [0, t_\varepsilon], \|W(t)\|_p \leq C_1 \varepsilon^\alpha + C_2 \varepsilon^{\alpha-1} \int_0^t \|W(s)\|_p ds. \quad (48)$$

By Gronwall's lemma we then have

$$\forall t \in [0, t_\varepsilon], \|W(t)\|_p \leq C_1 e^{C_2 T} \varepsilon^\alpha. \quad (49)$$

Similarly, we obtain

$$\dot{W}(t) = -\sin t W(0) + \cos t \dot{W}(0) + \int_0^t \cos(t-s) [N(W, R)](s) ds.$$

Using the same estimates as the ones involved in proving (48) and estimate (49), one can show that the above identity yields

$$\forall t \in [0, t_\varepsilon], \|\dot{W}(t)\|_p \leq C \varepsilon^\alpha. \quad (50)$$

Summing estimates (45), (47), (49), (50), we find that $\|X(t)\|_p = O(\varepsilon^\alpha) < M \varepsilon$ for all $t \in [0, t_\varepsilon]$ if ε is small enough. Consequently, the property (41) is not satisfied, which implies that (42) must hold instead. We therefore have

$$t_\varepsilon = T \varepsilon^{1-\alpha}$$

in estimates (45), (47), (49) and (50). Combining these estimates with the DpS error bound (32) and the assumption (28), we deduce the error bounds (24), (25) from the identities

$$\begin{aligned} u(t) - 2\varepsilon \operatorname{Re}(A(\varepsilon^{\alpha-1}t) e^{it}) &= W(t) + R(t) + Q_a(t) - 2\varepsilon \operatorname{Re}(A(\varepsilon^{\alpha-1}t) e^{it}), \\ \dot{u}(t) + 2\varepsilon \operatorname{Im}(A(\varepsilon^{\alpha-1}t) e^{it}) &= \dot{W}(t) + \dot{R}(t) + \dot{Q}_a(t) + 2\varepsilon \operatorname{Im}(A(\varepsilon^{\alpha-1}t) e^{it}), \\ v &= R - \sigma Q_a - \sigma W. \end{aligned}$$

This completes the proof of Theorem 3.1.

4 Time-periodic traveling waves

We now use the DpS equations to investigate time-periodic traveling wave solutions of our system. In what follows, it will be convenient to use the strain formulation (3) and also rewrite the DpS equation (17) in terms of strain-like variables

$$2i\kappa\omega^3\partial_\tau\delta^-A_n = \delta^+[h_\alpha(\delta^-B_n, |\delta^-A_n|)\delta^-A_n] - \delta^+[h_\alpha(\delta^-B_{n-1}, |\delta^-A_{n-1}|)\delta^-A_{n-1}]. \quad (51)$$

A special class of solution of (51), (18) has the form of a *periodic traveling wave*

$$\delta^-A_n(\tau) = ae^{i(\Omega\tau - qn - \phi)}, \quad \delta^-B_n(\tau) = b, \quad (52)$$

where the frequency Ω depends on the amplitude $a > 0$, the constant b and the wave number q through the nonlinear dispersion relation

$$\Omega = \frac{2}{\kappa\omega^3} \left| \sin \frac{q}{2} \right|^2 h_\alpha(b, a). \quad (53)$$

Note that definition of h_α in (16) requires that $b \leq 2\kappa a$. In particular, the dispersion relation has a closed form when $b = 0$. In fact, as shown in [15] for $\kappa = 1$, in this case

$$h_\alpha(0, r) = 2^{\alpha-1} c_\alpha \kappa^\alpha r^{\alpha-1}, \quad c_\alpha = \frac{1}{\pi} \frac{\Gamma(1/2)\Gamma(\alpha/2 + 1)}{\Gamma((\alpha + 1)/2 + 1)},$$

and the dispersion relation is given by

$$\Omega_0 = \frac{c_\alpha 2^\alpha (\kappa a)^{\alpha-1}}{\omega^3} \left| \sin \frac{q}{2} \right|^2.$$

Equations (8), (52) and (53) yield the following first-order approximation of the periodic traveling wave solutions of system (3):

$$x_n^{tw}(t) = \varepsilon b + 2\kappa\varepsilon a \cos(nq - \omega_{tw}t + \phi), \quad y_n^{tw}(t) = \varepsilon b - \frac{2\kappa\varepsilon a}{\rho} \cos(nq - \omega_{tw}t + \phi), \quad (54)$$

where ω_{tw} is the traveling wave frequency given by

$$\omega_{tw} = \Omega\varepsilon^{\alpha-1} + \omega = \omega + \frac{2\varepsilon^{\alpha-1}}{\kappa\omega^3} \left| \sin \frac{q}{2} \right|^2 h_\alpha(b, a). \quad (55)$$

To investigate how well the dynamics governed by the DpS equations approximates the traveling wave solutions of (3), we consider initial conditions determined from the first-order approximation (8):

$$\begin{aligned} x_n^{app}(t) &= \varepsilon\delta^-B_n(\varepsilon^{\alpha-1}t) + \kappa\varepsilon\delta^-A_n(\varepsilon^{\alpha-1}t)e^{i\omega t} + c.c. \\ y_n^{app}(t) &= \varepsilon\delta^-B_n(\varepsilon^{\alpha-1}t) - \frac{\kappa\varepsilon}{\rho}\delta^-A_n(\varepsilon^{\alpha-1}t)e^{i\omega t} + c.c. \end{aligned} \quad (56)$$

at $t = 0$, along with initial velocities given by

$$\begin{aligned} \dot{x}_n(0) &= \varepsilon\{\varepsilon^{\alpha-1}\delta^-\dot{B}_n(0) + \kappa\varepsilon^{\alpha-1}\delta^-\dot{A}_n(0) + i\kappa\omega\delta^-A_n(0) + c.c.\} \\ \dot{y}_n(0) &= \varepsilon\{\varepsilon^{\alpha-1}\delta^-\dot{B}_n(0) - \frac{\kappa}{\rho}\varepsilon^{\alpha-1}\delta^-\dot{A}_n(0) - i\frac{\kappa}{\rho}\omega\delta^-A_n(0) + c.c.\}. \end{aligned} \quad (57)$$

Here $\delta^-A_n(0)$ are set to be small perturbations of (52) at $\tau = 0$ and $\phi = 0$:

$$\delta^-A_n(0) = a[(1 + \zeta_n^{(1)}) \cos(nq) - i(1 + \zeta_n^{(2)}) \sin(nq)], \quad (58)$$

where $\zeta_n^{(1)}$ and $\zeta_n^{(2)}$ are uniformly distributed random variables in $[-\zeta, \zeta]$ with small $\zeta > 0$. Let $C = g_\alpha(b, |a|) > 0$ for given constants a and $b < 2\kappa|a|$. Then $\delta^-B_n(\tau)$ is determined from (18) by numerically solving

$$g_\alpha(\delta^-B_n(\tau), |\delta^-A_n(\tau)|) = C. \quad (59)$$

From the definition of g_α in (15), it is clear that the function $b \mapsto g_\alpha(b, r)$ is decreasing on $(-\infty, 2\kappa r)$ and satisfies $\lim_{b \rightarrow -\infty} g_\alpha(b, r) = +\infty$ and $g_\alpha(b, r) = 0$ for $b \geq 2\kappa r$. Consequently equation (59) admits a unique solution $\delta^-B_n(\tau) \in (-\infty, 2\kappa|\delta^-A_n(\tau)|)$. In particular, we obtain the value of $\delta^-B_n(0)$ by solving (59) at $\tau = 0$. Note that $\delta^-A_n(0)$ and $\delta^-B_n(0)$ can be computed exactly using DpS equations (51), (59), although their contribution is negligible since they correspond to higher order terms in the expression of initial velocities $\dot{x}_n(0)$ and $\dot{y}_n(0)$. In particular, when the perturbation is zero (i.e. $\zeta = 0$), the initial condition simplifies to

$$\begin{aligned} x_n(0) &= \varepsilon b + 2\varepsilon\kappa a \cos(nq + \phi), & y_n(0) &= \varepsilon b - \frac{2\varepsilon\kappa a}{\rho} \cos(nq + \phi), \\ \dot{x}_n(0) &= 2\omega_{tw}\kappa\varepsilon a \sin(nq + \phi), & \dot{y}_n(0) &= -\frac{2\omega_{tw}\kappa\varepsilon a}{\rho} \sin(nq + \phi). \end{aligned} \quad (60)$$

Integrating (3) numerically on a finite chain with these initial conditions and using periodic boundary conditions $x_0 = x_N$, $x_{N+1} = x_1$, we can compare the solution of (3) (referred to in what follows as the numerical solution) with the ansatz (54) when $\zeta = 0$ or the ansatz (56) when $\zeta > 0$. The latter is obtained by solving (51), (59) with periodic boundary conditions $\delta^-A_0(\tau) = \delta^-A_N(\tau)$, $\delta^-A_{N+1}(\tau) = \delta^-A_1(\tau)$, using the Runge-Kutta method and a standard numerical root finding routine to determine $\delta^-B_n(\tau)$ from (59) for given $\delta^-A_n(\tau)$ at each step.

4.1 Numerical traveling waves and the DpS approximation

We now consider a locally resonant chain with $N = 50$ masses. In what follows, we set $\kappa = 1$, noting that other values of this parameter can be recovered by the appropriate rescaling of time and amplitude. To investigate the accuracy of the DpS approximation of the small-amplitude traveling waves, we first fix mass ratio $\rho = 1/3$ and normalize the traveling wave solution (52) by fixing $a = 1$, $\phi = 0$ and $b = 1$. The linear frequency is given by $\omega = \sqrt{\kappa + \kappa/\rho} = 2$.

In the first numerical run, we set $q = \pi/5$, $\zeta = 0$ and consider the traveling wave with frequency $\omega_{tw} = \omega + 0.001$, so that $\varepsilon \approx 0.057$ from the nonlinear dispersion relation (55). Equation (54) then yields the amplitude of x_n^{tw} approximately equal to 0.114, which corresponds to the small-amplitude regime. As shown in the left panel of Fig. 1, the agreement between the numerical and approximate solutions is excellent, even after a long time

$t = 100 T_{tw}$, where $T_{tw} = 2\pi/\omega_{tw} = 3.126$ is the period of the traveling wave. The relative errors of the approximate solutions

$$E_x(t) = \frac{1}{2\varepsilon\kappa a} \|x_n^{app}(t) - x_n(t)\|_\infty \quad \text{and} \quad E_y(t) = \frac{\rho}{2\varepsilon\kappa a} \|y_n^{app}(t) - y_n(t)\|_\infty \quad (61)$$

are less than 8% at the final time of computation and remain bounded throughout the reported time evolution, as shown in the right panel of Fig. 1. In the second numerical run,

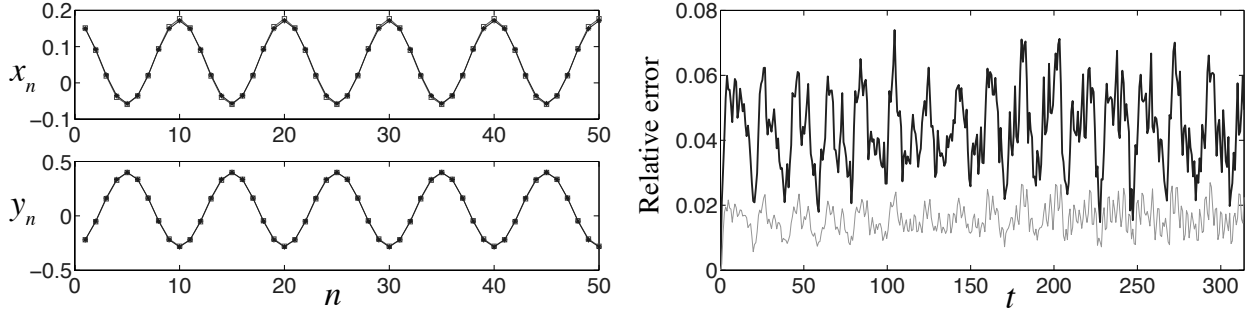


Figure 1: Left plot: strain profiles of small-amplitude approximate solution (54) (connected stars) and numerical solution of (3) (connected squares) at $t = 100 T_{tw} \approx 314$. Right plot: the relative errors $E_x(t)$ (black curve) and $E_y(t)$ (grey curve) of the DpS approximation. Here $\phi = 0$, $k = 1$, $q = \pi/5$, $b = 1$, $a = 1$, $\zeta = 0$ and $\omega_{tw} = w + 0.001$.

we set $\zeta = 0.01$ for the perturbation in (58), while the other parameters remain the same. The agreement between the numerical and approximate solutions is still excellent over the same time interval (see the left plot of Fig. 2). Moreover, the right plot of Fig. 2 shows the normalized differences

$$\tilde{E}_x(t) = \frac{1}{2\varepsilon\kappa a} \|x_n^{ptd}(t) - x_n(t)\|_\infty \quad \text{and} \quad \tilde{E}_y(t) = \frac{\rho}{2\varepsilon\kappa a} \|y_n^{ptd}(t) - y_n(t)\|_\infty \quad (62)$$

between a perturbed traveling wave (x_n^{ptd}, y_n^{ptd}) (numerical solution obtained for the perturbed initial condition) and the unperturbed numerical traveling wave solution (x_n, y_n) shown in Fig. 1 with the wave number $q = \pi/5$. As shown by Fig. 2, the initial perturbation is not amplified at the early stage of the numerical integration of (3) (for $t \leq 50 \approx 16 T_{tw}$). However, the subsequent growth of perturbations indicates the instability of the traveling wave solution.

In the next computation, we increase the wave number up to $q = 4\pi/5$ and keep all the other parameters the same as before. Now the asymptotic scale becomes quite small as $\varepsilon \approx 6.37 \times 10^{-4}$, which yields a very small amplitude of $x_n^{tw} \approx 0.0013$. As shown in Fig. 3, the DpS equations can successfully capture the dynamics of the small-amplitude traveling wave solution of the original system. In addition, the small-amplitude traveling wave with $q = 4\pi/5$ appears to be stable on the interval $t \in [0, 600]$. However, this result may be linked with the very small traveling wave amplitude, and instabilities might appear on longer time scales.

It is worth pointing out that the time scale of the validity of the DpS approximation depends not only on the asymptotic scale ε but also on the wave number q . To illustrate

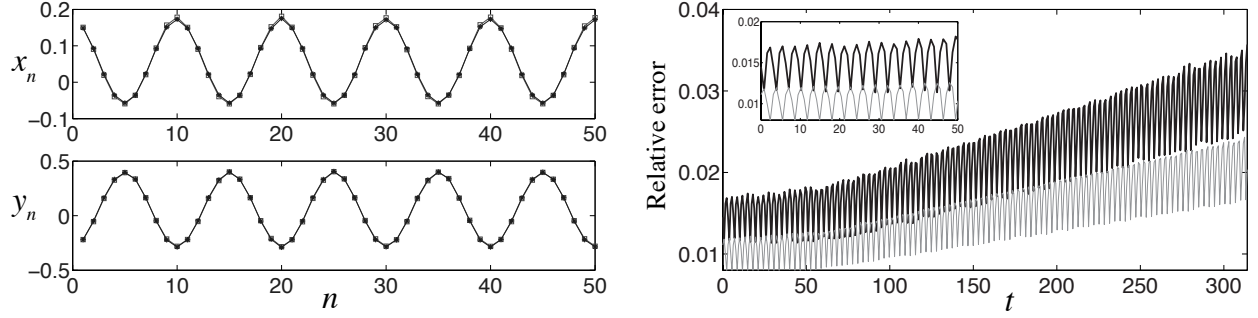


Figure 2: Left plot: strain profiles of small-amplitude approximate solution (connected stars) from the ansatz (56) and perturbed traveling wave solution (connected squares) at $t = 100 T_{tw} \approx 314$. Right plot: the normalized differences $\tilde{E}_x(t)$ (black curve) and $\tilde{E}_y(t)$ (grey curve) of the perturbed traveling wave and the unperturbed solution shown in Fig. 1. Here $\zeta = 0.01$ and all the other parameters are the same as in Fig. 1. A growth of the perturbations can be clearly observed in the dynamics.

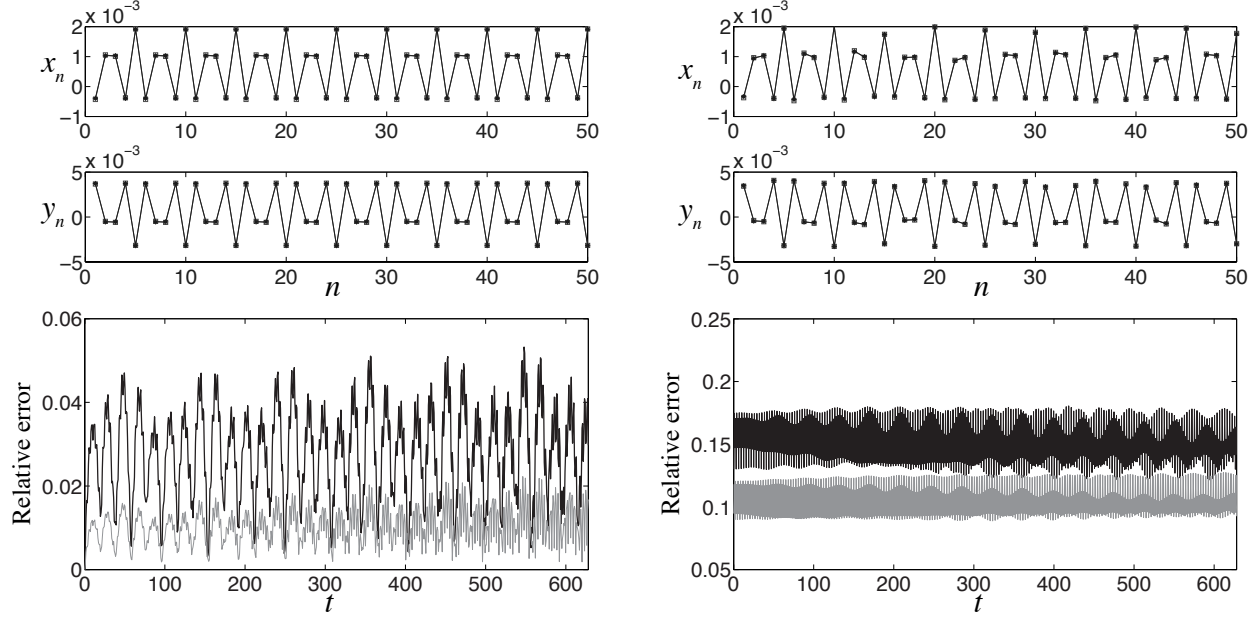


Figure 3: Top panels: strain profiles of small-amplitude approximate solution (connected stars) from the ansatz (56) and numerical results (connected squares) with both unperturbed (left) and perturbed initial conditions with $\zeta = 0.1$ (right) at $t = 200 T_{tw} \approx 628$, respectively. Bottom panels: left plot shows the relative errors $E_x(t)$ (black curve) and $E_y(t)$ (grey curve) of the DpS approximation. Right plot shows the normalized differences $\tilde{E}_x(t)$ (black curve) and $\tilde{E}_y(t)$ (grey curve) between the perturbed and unperturbed traveling waves. Here $q = 4\pi/5$ and all the other parameters are the same as in Fig. 1.

this, we first consider the wave number $q = \pi/5$ but increase the traveling wave frequency up to $\omega_{tw} = \omega + 0.003$, which yields $\varepsilon \approx 0.514$ and the amplitude of x_n^{tw} around 1.028. As revealed by the left plot in Fig. 4, the DpS equations fail to describe the dynamics of (3) appropriately soon after we start the integration. We then increase the wave number up to $q = 4\pi/5$ but choose $\omega_{tw} = \omega + 0.009$ yielding $\varepsilon \approx 0.0516$, which is even smaller than the asymptotic scale ε used in Fig. 1. However, notable difference between the traveling wave patterns of the numerical and approximate solutions are observed over the same time interval $[0, 314]$ (see the right plot of Fig. 4).

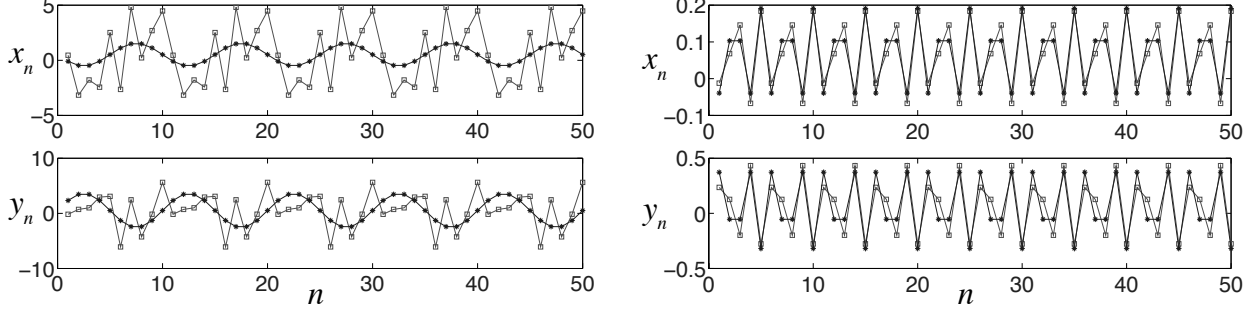


Figure 4: Left panel: results of the simulations with the same parameters as in Fig. 1 except for $\omega_{tw} = \omega + 0.003$ and the snapshot is taken at $t = 10T_{tw} \approx 31.4$. Right panel: results of the simulations with the same parameters as in the left panels of Fig. 3 except for $\omega_{tw} = \omega + 0.009$ and the snapshot is taken at $t = 314$.

4.2 Effect of mass ratio ρ

To investigate the effect of the mass ratio ρ on the validity of the DpS approximation of the small-amplitude traveling waves, we fix $q = \pi/5$, $\varepsilon = 0.01$ and keep the other parameters the same as before. We choose mass ratio $\rho = 3$ and the traveling wave frequency in (55) is now given by $\omega_{tw} \approx \omega + 0.002$, where the linear frequency is $\omega = 1.1547$. The results of the simulations are shown in Fig. 5. We observe again that the agreement between the numerical and approximate solutions remains excellent over the time interval $[0, 100T_{tw}]$, and the numerical traveling waves appear to be stable over the time interval $[0, 100]$. However, we note the growing trend of the difference between the perturbed and unperturbed traveling wave solutions after $t \approx 100$, which illustrates the instability of the traveling wave.

We further increase ρ to the critical value $\rho_c = \varepsilon^{1-\alpha} = 10$. The linear and traveling wave frequencies are given by $\omega = 1.0488$ and $\omega_{tw} = 1.0517$, respectively. As shown by the left panel of Fig. 6, the wave form of y_n is no longer sinusoidal at $t = 100T_{tw}$, while the wave form of x_n remains sinusoidal and matches its DpS approximation very well over the time interval $[0, 100T_{tw}]$. We observe also a growing trend in the relative error between the numerical and approximate solutions, despite the structural similarities of the profiles. To investigate the case when ρ is large ($O(\varepsilon^{1-\gamma})$, $\gamma > \alpha$), we now set $\rho = 1000$ and keep all other parameters the same as before. The linear frequency is now given by $\omega = 1.0005$ and approximate frequency is $\omega_{tw} = 1.0038$. Again, over the integration time interval $[0, 100T_{tw}]$ the wave form of x_n remains sinusoidal and close to the ansatz (54) but the waveform of y_n is non-sinusoidal and significantly deviates from the DpS traveling wave approximation

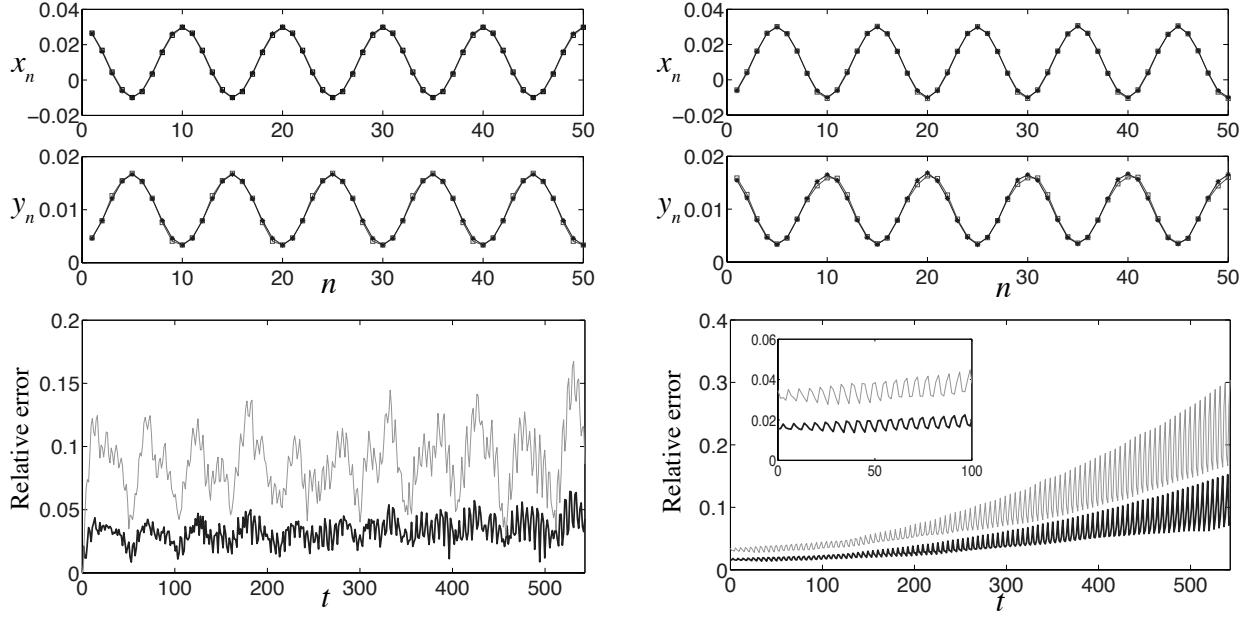


Figure 5: Results of the simulations with the same parameters as in Fig. 3 except for $\rho = 3$, $q = \pi/5$ and $\varepsilon = 0.01$. The strain profiles of both panels correspond to snapshots taken at $t = 100 T_{tw}$ and the perturbation added in the initial condition is $\zeta = 0.01$.

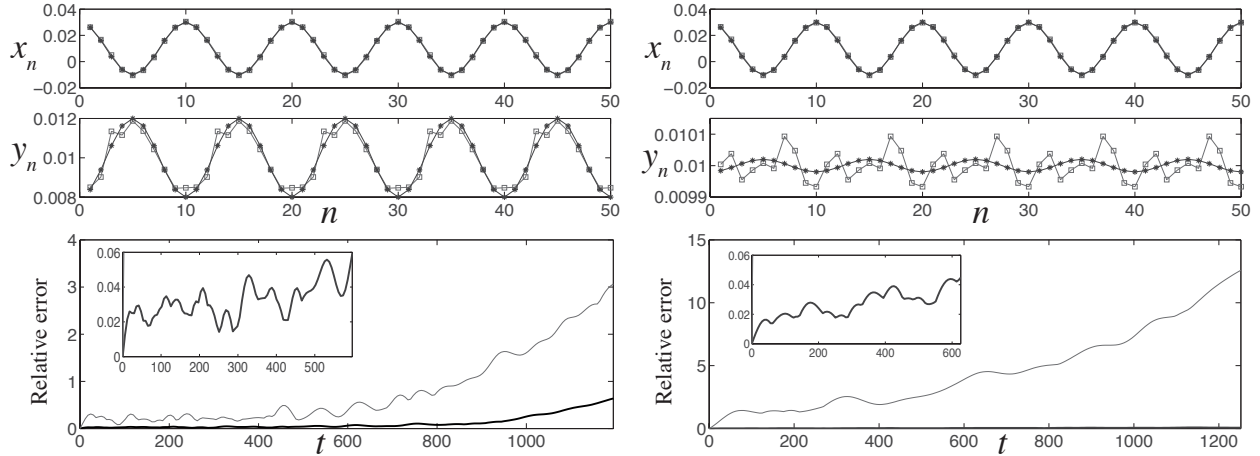


Figure 6: Results of the simulations with the same parameters as in the left panel of Fig. 5 except for $\rho = 10$ (left panel) and $\rho = 1000$ (right panel). The strain profiles of both panels correspond to the snapshot taken at $t = 100 T_{tw}$. The insets in the bottom plots show the enlarged plots of the relative error $E_x(t)$.

(see the right plots in Fig. 6). These results are consistent with the discussion in Sec. 3.1, since the derivation of the DpS equations (17)-(18) requires that ρ is below the critical value $\rho_c = \varepsilon^{1-\alpha}$ for given ε . Note that if we further set $b = 0$, the DpS equation (17) reduces to the one capturing the traveling waves in Newton's cradle problem in [15]. Numerical results (not reported here) reveal that the numerical solution of x_n is sinusoidal and very well approximated by the traveling wave ansatz (54). However, the difference between exact and approximate solutions of y_n is very substantial. Here the structural characteristics of the solution for y_n are no longer properly captured by the DpS approximation.

These numerical simulations reveal that the validity of the DpS approximation at fixed wave number q is very sensitive to the mass ratio ρ . When ρ is relatively small, the generalized DpS equations (17)-(18) successfully capture the dynamics of periodic traveling waves. When $\rho \geq \rho_c = \varepsilon^{1-\alpha}$, an increasing deviation between the exact and approximate solutions of y_n emerges. However, in all cases, the agreement of approximate and numerical solutions for x_n remains excellent over a finite time interval. In addition, traveling wave instabilities can be observed depending on the values of ρ , wave number q , wave amplitude and time scales considered.

5 Bright Breathers

Bright breathers are time-periodic solutions of (2) which converge to constants (zero strain) at infinity, i.e.

$$u_n, v_n \rightarrow c_{\pm}, \quad \text{as } n \rightarrow \pm\infty \quad (63)$$

uniformly in time. In this section we examine the existence of either exact or *long-lived* bright breather solutions of (2). The second class of solutions refers to spatially localized solutions of (2) remaining close to a time-periodic oscillation over long times.

We begin by noting the existence of trivial exact bright breather solutions of (2) for which particles do not interact, i.e. $(u_{n-1}(t) - u_n(t))_+^\alpha = 0$ for all t and n . This is equivalent to having

$$u_{n-1}(t) \leq u_n(t) \quad \forall t \in \mathbb{R}, \forall n \in \mathbb{Z}, \quad (64)$$

$$\begin{aligned} \ddot{u}_n &= \kappa(v_n - u_n), \\ \rho \ddot{v}_n &= \kappa(u_n - v_n). \end{aligned} \quad (65)$$

The time-periodic solutions of (65) read

$$u_n(t) = \frac{\rho}{1+\rho} a_n \cos(\omega t + \phi_n) + b_n, \quad v_n(t) = -\frac{1}{1+\rho} a_n \cos(\omega t + \phi_n) + b_n, \quad (66)$$

where we can fix $a_n \geq 0$ and denote $\omega^2 = \kappa(1 + 1/\rho)$. Bright breather profiles are obtained for

$$\lim_{n \rightarrow \pm\infty} a_n = 0, \quad \lim_{n \rightarrow \pm\infty} b_n = c_{\pm}. \quad (67)$$

A solution of (2) is obtained if and only if the constraint (64) is satisfied, which is equivalent to

$$b_n - b_{n-1} \geq \frac{\rho}{1+\rho} [a_n^2 + a_{n-1}^2 - 2a_n a_{n-1} \cos(\phi_n - \phi_{n-1})]^{1/2} \quad \forall n \in \mathbb{Z}. \quad (68)$$

For $(a_n)_{n \in \mathbb{Z}} \in \ell_1(\mathbb{Z})$, this is equivalent to assuming

$$b_n = d_n + \frac{\rho}{1+\rho} \sum_{k=-\infty}^n [a_k^2 + a_{k-1}^2 - 2a_k a_{k-1} \cos(\phi_k - \phi_{k-1})]^{1/2},$$

where $(d_n)_{n \in \mathbb{Z}}$ is a nondecreasing sequence converging as $n \rightarrow \pm\infty$. It is clear from this expression that $(b_n)_{n \in \mathbb{Z}}$ corresponds to a kink profile. Moreover, fixing $\phi_n - \phi_{n-1} = \pi$, we can simplify the above expression to obtain

$$b_n = d_n + \frac{\rho}{1+\rho} \left(a_n + 2 \sum_{k=-\infty}^{n-1} a_k \right).$$

We now prove the following.

Theorem 5.1 *The trivial bright breather solutions defined by (66)-(67)-(68) are the only time-periodic bright breather solutions of (2).*

To prove Theorem 5.1, we follow the method of the proof of nonexistence of breathers in FPU chains with repulsive interactions given in [16]. Suppose (u_n, v_n) is a bright breather, i.e. a T -periodic solution of (2) satisfying (63). Adding the equations in (2), one can see that the bright breather solution must satisfy

$$\ddot{u}_n + \rho \ddot{v}_n = (u_{n-1} - u_n)_+^\alpha - (u_n - u_{n+1})_+^\alpha. \quad (69)$$

Integrating (69) over one period, we obtain

$$\bar{F}_{n+1} = \bar{F}_n, \quad \bar{F}_n = \frac{1}{T} \int_0^T (u_{n-1}(t) - u_n(t))_+^\alpha dt. \quad (70)$$

Note that $\bar{F} = \bar{F}_n$ is independent of n and one can show that it vanishes. Indeed, by (63), we have

$$\lim_{n \rightarrow \pm\infty} \|u_n - u_{n-1}\|_{L^\infty(0,T)} = 0. \quad (71)$$

Meanwhile,

$$|\bar{F}| = \frac{1}{T} \int_0^T (u_{n-1}(t) - u_n(t))_+^\alpha dt \leq \|u_{n-1}(t) - u_n(t)\|_{L^\infty(0,T)}^\alpha \quad (72)$$

for all n . Taking the limit $n \rightarrow \pm\infty$ in (72) one obtains $\bar{F} = 0$. Consequently, for each n , we have

$$\int_0^T (u_{n-1}(t) - u_n(t))_+^\alpha dt = 0 \quad (73)$$

and since $F_n = (u_{n-1} - u_n)_+^\alpha$ is non-negative, continuous and T -periodic, we have $F_n = 0$ for all t and n . Thus (u_n, v_n) satisfies the linear system (65) and corresponds to a trivial bright breather solution. This completes the proof of Theorem 5.1.

In what follows we show that, although nontrivial time-periodic bright breathers do not exist for system (2), long-lived small-amplitude bright breather solutions can be found when ρ is large. This is due to the connection between (2) and the DpS equation (20) established in section 3.2. Equation (20) admits time-periodic solutions of the form

$$A_n(\tau) = \varepsilon a_n e^{i\omega_0 |\varepsilon|^{\alpha-1} \tau}, \quad (74)$$

where $a = (a_n)_{n \in \mathbb{Z}}$ is a real sequence and $\varepsilon \in \mathbb{R}$ an arbitrary constant, if and only if a satisfies

$$a = -\delta^+ [|\delta^- a|^{\alpha-1} \delta^- a]. \quad (75)$$

In particular, nontrivial solutions of (75) satisfying $\lim_{n \rightarrow \pm\infty} a_n = 0$ correspond to bright breather solutions of (20) given by (74). These solutions are doubly exponentially decaying, so that they belong to ℓ_p for all $p \in [1, \infty]$. They have been studied in a number of works (see [25] and references therein). The following existence theorem for spatially symmetric breathers has been proved in [25] using a reformulation of (75) as a two-dimensional mapping.

Theorem 5.2 *The stationary DpS equation (75) admits solutions a_n^i ($i = 1, 2$) satisfying*

$$\lim_{n \rightarrow \pm\infty} a_n^i = 0,$$

$$\begin{aligned} (-1)^n a_n^i &> 0, \quad |a_n^i| > |a_{n-1}^i| \quad \text{for all } n \leq 0, \\ \text{and } a_n^1 &= a_{-n}^1, \quad a_n^2 = -a_{-n+1}^2, \quad \text{for all } n \in \mathbb{Z}. \end{aligned}$$

Furthermore, for all $\beta \in (0, 1)$, there exists $n_0 \in \mathbb{N}$ such that the above-mentioned solutions a_n^i satisfy, for $i = 1, 2$:

$$\forall n \geq n_0, \quad |a_n^i| \leq \beta^{1+\alpha^{n-n_0}}.$$

Considering the bright breather solutions of (20) given by (74) with $a = a^i$, $\varepsilon = 1$, and applying Theorem 3.1, one obtains stable exact solutions of equations (2), close to the bright breathers, over the corresponding time scales. This yields the following result formulated for $\kappa = 1$.

Theorem 5.3 *Fix constants $C_r, C_i, T > 0$. Consider a solution $a^i = (a_n^i)_{n \in \mathbb{Z}}$ ($i = 1, 2$) of the stationary DpS equation (75) described in Theorem 5.2. There exist $\varepsilon_T, C_T > 0$ such that for all $\varepsilon \in (0, \varepsilon_T]$ and for $\rho^{-1} \leq C_r \varepsilon^{2(\alpha-1)}$, for all initial condition of (2) in ℓ_p^4 satisfying*

$$\|u(0) - 2\varepsilon a^i\|_p + \|\dot{u}(0)\|_p + \|v(0)\|_p \leq C_i \varepsilon^\alpha, \quad \|\dot{v}(0)\|_p \leq C_i \varepsilon^{2\alpha-1}, \quad (76)$$

the solution to equation (2) is defined at least for $t \in [0, T\varepsilon^{1-\alpha}]$ and satisfies

$$\|u(t) - 2\varepsilon a^i \cos(\Omega_b t)\|_p + \|\dot{u}(t) + 2\varepsilon a^i \sin(\Omega_b t)\|_p \leq C_T \varepsilon^\alpha, \quad \text{for all } t \in [0, T\varepsilon^{1-\alpha}], \quad (77)$$

with $\Omega_b = 1 + \omega_0 \varepsilon^{\alpha-1}$, ω_0 defined in (21) and

$$\|v(t)\|_p \leq C_T \varepsilon^\alpha, \quad \|\dot{v}(t)\|_p \leq C_T \varepsilon^{2\alpha-1}, \quad \text{for all } t \in [0, T\varepsilon^{1-\alpha}]. \quad (78)$$

It is important to stress the differences between the long-lived bright breather solutions provided by Theorem 5.3 and the trivial bright breathers analyzed at the beginning of this section. The oscillations described in Theorem 5.3 are nontrivial in the sense that Hertzian interactions do not vanish identically. In addition, they are truly localized (for $p < \infty$) whereas the trivial exact breathers are superposed on a nonvanishing kink component b_n . Moreover, the (approximate) frequency Ω_b of long-lived bright breathers satisfies $0 < \Omega_b - 1 = O(\varepsilon^{\alpha-1})$ for breathers with amplitude $O(\varepsilon)$. For trivial exact bright breathers, the frequency ω is independent of amplitude and satisfies $0 < \omega - 1 = O(1/\rho)$ when ρ is large. Under the assumptions of Theorem 5.3, we have $1/\rho = O(\varepsilon^{2(\alpha-1)})$ and thus $\Omega_b > \omega$ for ε small enough.

We now investigate the behavior of long-lived bright breathers numerically. Fixing $T = 2\pi/\omega_0 = 19.4158$, $C_r = C_i = 1$ and choosing $\varepsilon = 0.01$, we consider a locally resonant chain of $N = 40$ masses with the mass ratio $\rho = 1000$ so that the inequality $\rho^{-1} \leq C_r \varepsilon^{2(\alpha-1)}$ in Theorem 5.3 is satisfied. We then integrate the system (2) over a long time interval $[0, 80T]$, starting with initial conditions

$$u(0) = 2\varepsilon a^i, \quad v(0) = 0, \quad \dot{u}(0) = \dot{v}(0) = 0 \quad (79)$$

where a^i is the numerical solution of (75) obtained using the method in [16]. The numerical simulation yields spatially localized solutions of (2) that stay close to the time-periodic oscillation

$$\tilde{u}(t) = 2\varepsilon a^i \cos(\Omega_b t), \quad \dot{\tilde{u}}(t) = -2\varepsilon a^i \sin(\Omega_b t), \quad \tilde{v}(t) = \dot{\tilde{v}}(t) \equiv 0 \quad (80)$$

with $i = 2$ over the time interval $[0, T\varepsilon^{1-\alpha}] = [0, 194.158]$, as can be seen in the inset of the right panel of Fig 7. Note that the comparison is made at times corresponding to multiples of $T_b = 2\pi/\Omega_b = 6.0862$. To measure the relative difference of the numerical solution of (2) and the time-periodic oscillations (80), we define the rescaled ℓ_1 -norms as follows:

$$E_u(t) = \frac{\|u(t) - \tilde{u}(t)\|_1}{\varepsilon^\alpha}, \quad E_{\dot{u}}(t) = \frac{\|\dot{u}(t) - \dot{\tilde{u}}(t)\|_1}{\varepsilon^\alpha} \quad (81)$$

and

$$E_v(t) = \frac{\|v(t) - \tilde{v}(t)\|_1}{\varepsilon^\alpha}, \quad E_{\dot{v}}(t) = \frac{\|\dot{v}(t) - \dot{\tilde{v}}(t)\|_1}{\varepsilon^{2\alpha-1}}. \quad (82)$$

The fact that those rescaled norms remain small over time interval $[0, T\varepsilon^{1-\alpha}]$ is consistent with the result of Theorem 5.3 and confirms the existence of the long-lived bright breathers. However, at larger time, part of the energy is radiated away from the vicinity of the initially excited sites. As a result, we observe the breakdown of the localized structure for a long-time ($t \gg T\varepsilon^{1-\alpha}$) evolution, and the solution profile spreads out and eventually approaches a kink-type structure shown by circles in the left panel of Fig 7. This is associated with the growing magnitude of v_n during the simulation.

6 Approximate dark breather solutions

We now turn to dark breather solutions, which, as we will see, are fundamentally different from the waveforms considered in the previous section and are not excluded by the results

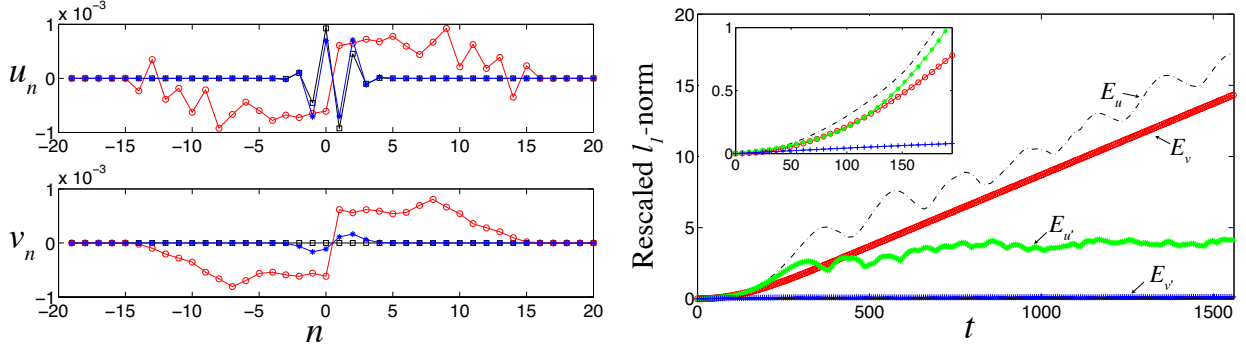


Figure 7: Left panels: snapshot of numerical solution of (2) at $t = 30T_b < 10T$ (blue stars) and $t = 80T$ (red circles), respectively, starting with initial conditions (79) with $i = 2$ (black squares). Right panel: time evolution of the rescaled ℓ_1 -norms defined in (81) and (82), where $E_u(t)$ is represented by connected dots (black curve), $E_{\tilde{u}}(t)$ by connected stars (green curve), $E_v(t)$ by connected circles (red curve) and $E_{\tilde{v}}(t)$ by connected pluses (blue curve). The inset in the right plot shows time evolution of the same ℓ_1 -norms when $t \leq T\epsilon^{1-\alpha}$.

of Theorem 5.1. To construct approximate dark breather solutions, we start by considering *standing wave* solutions of the generalized DpS equations (17)-(18) in the form

$$\delta^- A_n(\tau) = \delta^- a_n e^{i(\Omega\tau + \phi)} \quad (a_n \in \mathbb{R}), \quad \delta^- B_n(\tau) = \delta^- b_n, \quad (83)$$

where a_n and b_n are time-independent. Introducing $\omega_b = \omega + \Omega\epsilon^{\alpha-1}$, we find that the first-order approximate solution of (2) reads

$$\begin{aligned} u_n^{sw}(t) &= \epsilon b_n + 2\kappa\epsilon a_n \cos(\omega_b t + \phi), \\ v_n^{sw}(t) &= \epsilon b_n - \frac{2\kappa}{\rho}\epsilon a_n \cos(\omega_b t + \phi). \end{aligned} \quad (84)$$

Substituting (83) in the generalized DpS equations (17)-(18) we obtain

$$\begin{aligned} -\mu a_n &= h_\alpha(\delta^- b_{n+1}, |\delta^- a_{n+1}|) \delta^- a_{n+1} - h_\alpha(\delta^- b_n, |\delta^- a_n|) \delta^- a_n \\ \delta^+ g_\alpha(\delta^- b_n, |\delta^- a_n|) &= 0, \end{aligned} \quad (85)$$

where $\mu = 2\kappa\omega^3\Omega = 2\kappa\omega^3(\omega_b - \omega)\epsilon^{1-\alpha}$.

Following the approach in [15], for $\mu \neq 0$ one can further show that $\tilde{a}_n = |\mu|^{\frac{1}{1-\alpha}} a_n$, $\tilde{b}_n = |\mu|^{\frac{1}{1-\alpha}} b_n$ satisfy the renormalized equation

$$\begin{aligned} -\text{sign}(\mu)\tilde{a}_n &= h_\alpha(\delta^- \tilde{b}_{n+1}, |\delta^- \tilde{a}_{n+1}|) \delta^- \tilde{a}_{n+1} - h_\alpha(\delta^- \tilde{b}_n, |\delta^- \tilde{a}_n|) \delta^- \tilde{a}_n \\ \delta^+ g_\alpha(\delta^- \tilde{b}_n, |\delta^- \tilde{a}_n|) &= 0. \end{aligned} \quad (86)$$

where $\text{sign}(\mu) = 1$ for $\mu > 0$ and $\text{sign}(\mu) = -1$ for $\mu < 0$. For simplicity we drop the tilde in (86) in what follows. Numerical results suggest that a nontrivial solution for $\{\delta^- a_n\}$ can be found if and only if $\mu > 0$. Thus it suffices to consider the case $\mu = 1$. It is convenient to rewrite (86) in terms of $\delta^- a_n$ and $\delta^- b_n$ by subtracting from the first equation in (86) the

same equation at $n - 1$:

$$\begin{aligned}
-\delta^-a_n &= h_\alpha(\delta^-b_{n+1}, |\delta^-a_{n+1}|)\delta^-a_{n+1} - 2h_\alpha(\delta^-b_n, |\delta^-a_n|)\delta^-a_n + h_\alpha(\delta^-b_{n-1}, |\delta^-a_{n-1}|)\delta^-a_{n-1} \\
g_\alpha(\delta^-b_{n+1}, |\delta^-a_{n+1}|) &= g_\alpha(\delta^-b_n, |\delta^-a_n|).
\end{aligned} \tag{87}$$

We now use Newton's iteration to solve (87) numerically for $\delta^-a_n, \delta^-b_n, n = -N, \dots, N$, with periodic boundary conditions ($\delta^-a_{-N-1} = \delta^-a_N$ and $\delta^-a_{N+1} = \delta^-a_{-N}$). Note that the associated Jacobian matrix is singular due to the structure of second equation in (87), and therefore an additional constraint is necessary. It is sufficient to fix $\delta^-b_{-N} = c$, where c is a constant. Since we are looking for dark breathers, it is natural to consider initial values of δ^-a_n in the form

$$\delta^-a_n^0 = (-1)^n \tanh(n - n_0) \tag{88}$$

where n_0 is an arbitrary constant corresponding to spatial translation. One can then use the second equation in (87) to solve for initial guess of $\delta^-b_n^0, n = -N + 1, \dots, N$. A standard Newton's iteration procedure of the system (87) with $4N + 1$ variables $\delta^-b_{-N+1}, \dots, \delta^-b_N, \delta^-a_{-N}, \dots, \delta^-a_N$ is then performed with the tolerance of 10^{-8} . Setting $n_0 = 0$ in (88) results in a site-centered solution shown in the left panel of Fig. 8, whereas the bond-centered solution corresponds to $n_0 = 1/2$ shown the right panel. Typical breather waveforms of both bright [12] and dark [18] type come in these two broad families [10].

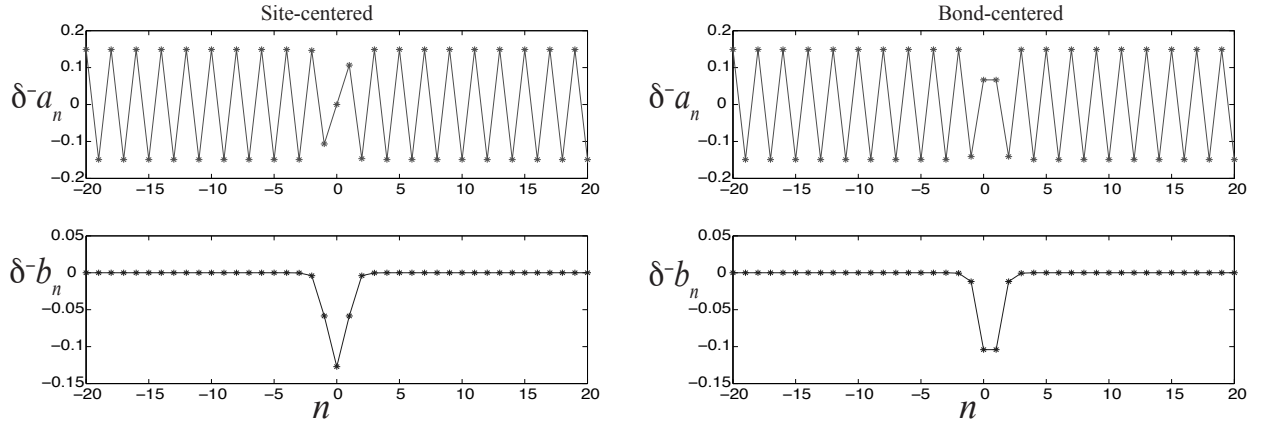


Figure 8: Left panel: A site-centered solution of (87) with $\delta^-b_{-N} = c = 0$. Right panel: bond-centered solution.

Once the Newton's iteration converges to a fixed point $\{(\delta^-a_n^*, \delta^-b_n^*)\}$, we can compute the first-order approximate solution of (3) given by

$$\begin{aligned}
x_n^{sw}(t) &= |\bar{\mu}|^{\frac{1}{\alpha-1}} \{\delta^-b_n^* + 2\kappa\delta^-a_n^* \cos(\omega_b t + \phi)\}, \\
y_n^{sw}(t) &= |\bar{\mu}|^{\frac{1}{\alpha-1}} \{\delta^-b_n^* - \frac{2\kappa}{\rho}\delta^-a_n^* \cos(\omega_b t + \phi)\},
\end{aligned} \tag{89}$$

where $\bar{\mu} = 2\kappa\omega^3(\omega_b - \omega)$.

7 Numerically exact dark breathers and linear stability analysis

Having constructed the initial seed (89), we can compute the numerically exact dark breather solution of system (3) with periodic boundary conditions. Let $x(t)$, $y(t)$, $\dot{x}(t)$ and $\dot{y}(t)$ denote the row vectors with component $x_n(t)$, $y_n(t)$, $\dot{x}_n(t)$ and $\dot{y}_n(t)$, respectively. Let $Z(t) = (x(t), y(t))$. We seek time-periodic solutions $(Z(t), \dot{Z}(t))$ of the Hamiltonian system (3) satisfying the initial conditions $(Z(0), \dot{Z}(0))$. For a fixed period of the dark breather solution given by $T_b = 2\pi/\omega_b$, where ω_b is the breather frequency, the problem is equivalent to finding the fixed points of the corresponding Poincaré map $P_{T_b}[(Z(0), \dot{Z}(0))^T] = (Z(T_b), \dot{Z}(T_b))^T$. Since the system (3) has the time-reversal symmetry, we can further restrict the solution space by setting $\dot{Z}(0) \equiv 0$.

We use a Newton-type algorithm (see, for example, Algorithm 2 in [30]) to compute the fixed point. More precisely, let $\Delta Z(0)$ be the small increment of the initial data that needs to be determined. It is then sufficient to minimize $\|P_{T_b}[(Z(0) + \Delta Z(0), 0)^T] - (Z(0) + \Delta Z(0), 0)^T\|$ at each iteration step. Notice that $P_{T_b}[(W(0), 0)^T]$ can be approximated by $P_{T_b}[(Z(0), 0)^T] + M(T_b)(\Delta Z(0), 0)^T$ for sufficiently small $\Delta Z(0)$. Here $M(t)$ is the associated monodromy matrix of the variational equations satisfying

$$\frac{d}{dt}M(t) = \mathcal{J}(Z(t), \dot{Z}(t))M(t), \quad M(0) = I, \quad (90)$$

where $\mathcal{J}(Z(t), \dot{Z}(t))$ is the Jacobian matrix of the nonlinear system (3) at $(Z(t), \dot{Z}(t))$, and I is the identity matrix. The Jacobian for the Newton's iteration is then given by $I - M(T_b)$ and it is singular since it can be shown that $M(T_b)$ has an eigenvalue pair equal to 1. To remove the singularity, we impose the additional constraint that the time average of $x_1(t) + \Delta x_1(t)$, the first component $Z(t) + \Delta Z(t)$, is fixed to be (approximately) zero. Observing that $(Z(t) + \Delta Z(t), \dot{Z}(t) + \Delta \dot{Z}(t))^T \approx (Z(t), \dot{Z}(t))^T + M(t)(Z(0), 0)^T$, we obtain

$$\frac{1}{T_b} \int_0^{T_b} x_1(t) dt + \frac{1}{T_b} \int_0^{T_b} M_1(t) \cdot \Delta Z(0) dt = 0, \quad (91)$$

where $M_1(t)$ is the first row of $M(t)$.

In the results discussed below we set $\kappa = 1$. To characterize the solution, we define the vertical centers of the solution for x and y components [18],

$$C_x = \frac{\sup_{t \in [0, T_b]} x_1(t) + \inf_{t \in [0, T_b]} x_1(t)}{2}, \quad C_y = \frac{\sup_{t \in [0, T_b]} y_1(t) + \inf_{t \in [0, T_b]} y_1(t)}{2} \quad (92)$$

and the amplitudes of the breather,

$$K_x = \frac{\sup_{t \in [0, T_b]} x_1(t) - \inf_{t \in [0, T_b]} x_1(t)}{2}, \quad K_y = \frac{\sup_{t \in [0, T_b]} y_1(t) - \inf_{t \in [0, T_b]} y_1(t)}{2}. \quad (93)$$

Note that the vertical center C_x is approximately zero due to the constraint (91). However, one can fix any other value of C_x by replacing zero in the right hand side of (91) by C_x . To

further investigate the long-term behavior of the dark breather solution, we introduce the relative error

$$E_b(t) = \|Z(mT_b) - Z(0)\|_\infty / \|Z(0)\|_\infty \quad (94)$$

where $m = \lfloor t/T_b \rfloor$ and $Z(mT_b) = (x(mT_b), y(mT_b))$ represents the strain profile after integrating (3) over m multiple of time periods, starting with the static dark breather $Z(0)$ as the initial condition.

We first consider the mass ratio $\rho = 1/3$, so that the linear frequency is $\omega = 2$. We choose a value of ω_b that is slightly greater than this value but close enough to it in order to obtain a good initial seed with a small amplitude. Once the Newton-type solver converges to a numerically exact dark breather solution, we use the method of continuation to obtain an entire family of dark breathers that corresponds to different values of ω_b . Sample profiles of both bond-centered and site-centered dark breather solutions with $\omega_b = 2.05$ along with the DpS approximate solutions (89) are shown in Fig. 9. The amplitudes K_x and K_y increase with ω_b , and the solution approaches zero as $\omega_b \rightarrow \omega$.

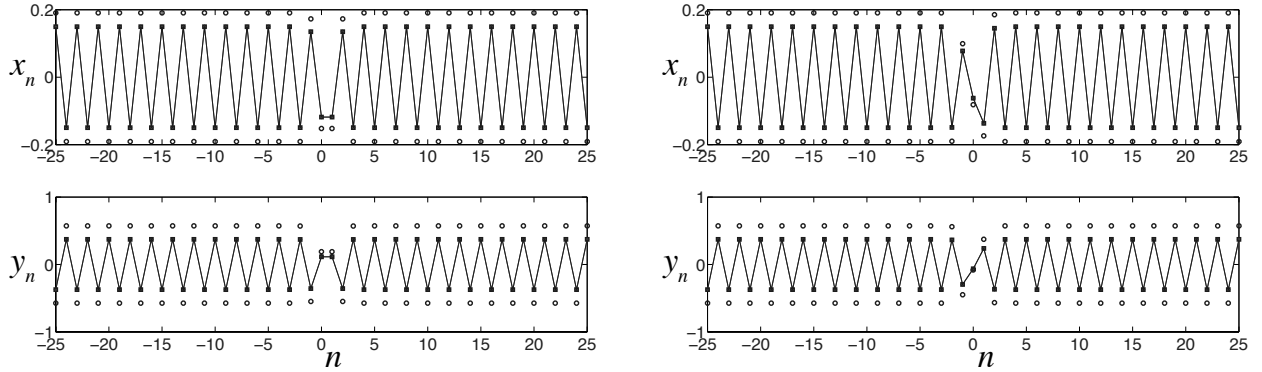


Figure 9: Left panel: a bond-centered solution of dark breather solution (connected stars) with frequency $\omega_b = 2.05$. Connected squares represent strain profile after integration over T_b and circles represent the DpS approximate solution from the ansatz (89). Right panel: site-centered solution. The relative errors $E_b(T_b)$ of both site-centered and bond-centered solutions are less than 4.5×10^{-9} . Here $\kappa = 1$ and $\rho = 1/3$.

The linear stability of each obtained dark breather solution is examined via a standard Floquet analysis. The eigenvalues (Floquet multipliers) of the associated monodromy matrix $M(T_b)$ determine the linear stability of the breather solution. The moduli of Floquet multipliers for the site-centered and bond-centered solutions of various frequencies are shown in Fig. 10, along with the numerically computed Floquet spectrum that corresponds to the sample breather profile at $\omega_b = 2.09$. If any of these Floquet multipliers λ_i satisfies $|\lambda_i| > 1$, the corresponding breather is linearly unstable. We observed two types of instabilities in this Hamiltonian system. The first one is the *real instability*, which corresponds to a real Floquet multiplier with magnitude greater than one; an example is shown in the right top plot in Fig. 10 for the bond-centered dark breather with $\omega_b = 2.09$. The second type is the *oscillatory instability*, which corresponds to a quartet of Floquet multipliers outside the unit circle with non-zero imaginary parts (see the right bottom plot of Fig. 10 for the site-centered dark breather with $\omega_b = 2.09$).

Numerical results reveal that the site-centered dark breathers appear to exhibit only oscillatory instabilities. These marginally unstable modes emerge at the beginning of the

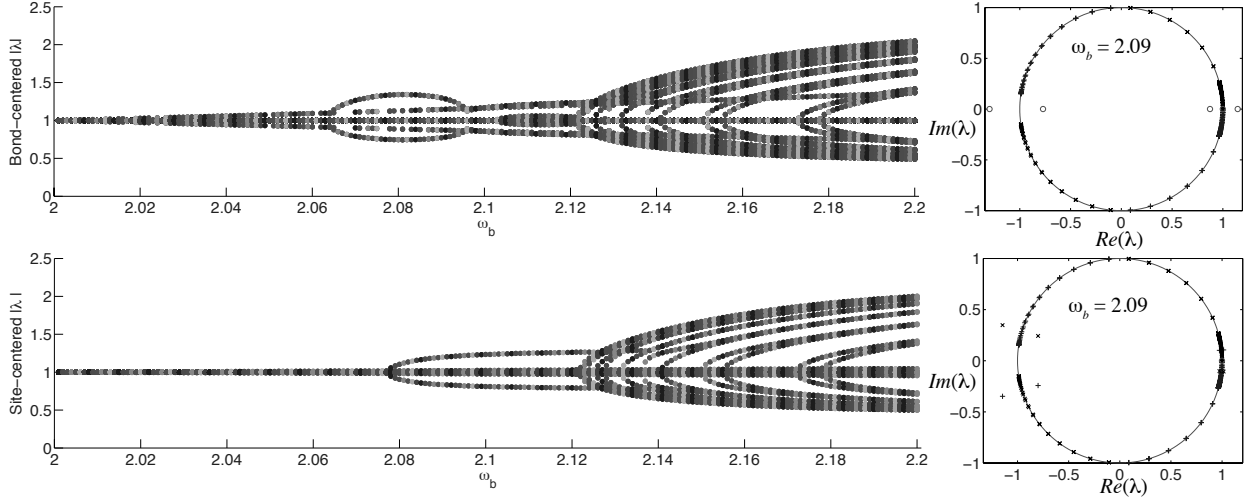


Figure 10: Left plots: moduli of the Floquet multipliers versus frequency ω_b for the bond-centered (top) and site-centered (bottom) breathers. The Floquet multipliers for $\omega_b = 2.09$ in the complex plane are shown in the respective plots on the right. Here $\kappa = 1$ and $\rho = 1/3$.

continuation procedure but remain weak until ω_b reaches $\omega_b \approx 2.078$. As shown in the right plot of Fig. 11, the relative error $E_b(1200)$ stays below 7×10^{-7} when $\omega_b \leq 2.077$ but increases dramatically afterwards. The results are consistent with the Floquet spectrum shown in the left plot of Fig. 11. In fact, beyond the critical point of $\omega_b \approx 2.078$, we observe the emergence of a new and stronger oscillatory instability mode that corresponds to two pairs of Floquet multipliers distributed symmetrically outside the unit circle around -1 (see also the right bottom plot of Fig. 10 for $\omega_b = 2.09$). Representative space-time evolution diagrams of site-centered dark breather solutions are shown in Fig. 12, which suggests that the site-centered dark breather solutions with frequency close to the linear frequency ω are long-lived and have marginal oscillatory instability, below the pertinent critical point. However, the oscillatory instability becomes more and more significant as ω_b increases, leading to the breakdown of the dark breather structure of the solution. In fact, beyond the critical point, the breakup of the site-centered breather appears to be accompanied in Fig. 12 by a dramatic evolution, whereby the configuration is completely destroyed and a form of lattice dynamical turbulence ensues. This phenomenon is reminiscent of traveling wave instabilities observed in [31] for Hertzian chains and may be worth further study, which, however, is outside the scope of the present manuscript.

In contrast to the site-centered solutions, the bond-centered ones exhibit only real instability at the early stage of the continuation when the breather frequency ω_b is greater than but close to ω . At those frequencies, the magnitude of the Floquet multipliers corresponding to the real instability of bond-centered breathers is larger than the moduli of the multipliers describing the oscillatory instability of the site-centered ones, resulting in not only shorter lifetime of the bond-centered solutions, but also setting the dark breather state in motion. A representative space-time evolution diagram for bond-centered dark breather solution of frequency $\omega_b = 2.05$ is shown in the left panel of Fig. 13. In the right panel of Fig. 13 the manifestation of real instability of the same solution is shown, where the perturbation of the dark breather solution along the direction associated with the unstable mode that

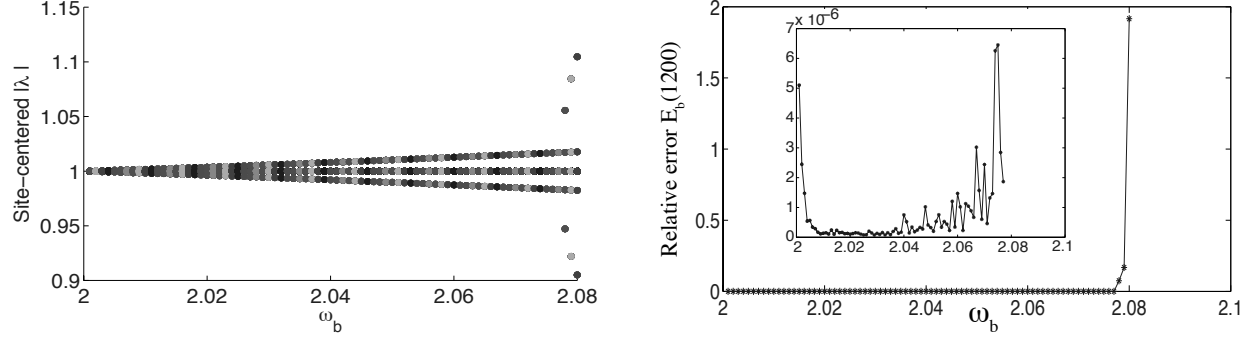


Figure 11: Left plot: moduli of the Floquet multipliers of the site-centered breathers for frequency $\omega_b \leq 2.08$. Right plot: the relative error $E_b(t)$ versus frequency at $t = 1200$. Inset shows the relative error for frequencies less than $\omega_b \leq 2.077$. Here $\kappa = 1$ and $\rho = 1/3$.

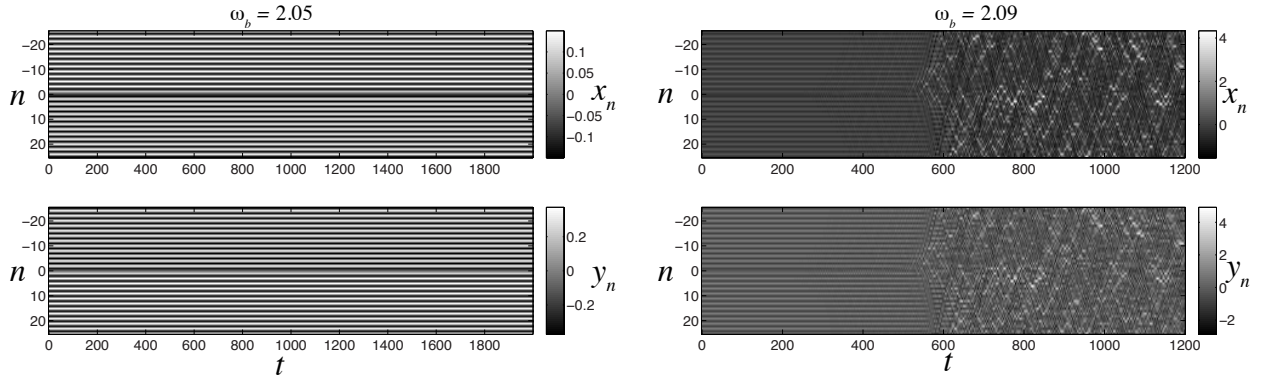


Figure 12: Left panel: contour plot of the time evolution of the site-centered solution for $\omega_b = 2.05$. The color bar corresponds to the magnitude of the strain x_n (top) and y_n (bottom). Right panel: same computation as in left panel but for $\omega_b = 2.09$. Here $\kappa = 1$ and $\rho = 1/3$.

corresponds to a real Floquet multiplier is used as the initial condition for the integration. One can see that the instability results in a dark breather moving with constant velocity after some initial transient time in the left panel, while the pertinent motion is initiated essentially immediately by the perturbation induced in the right panel. However, as ω_b is

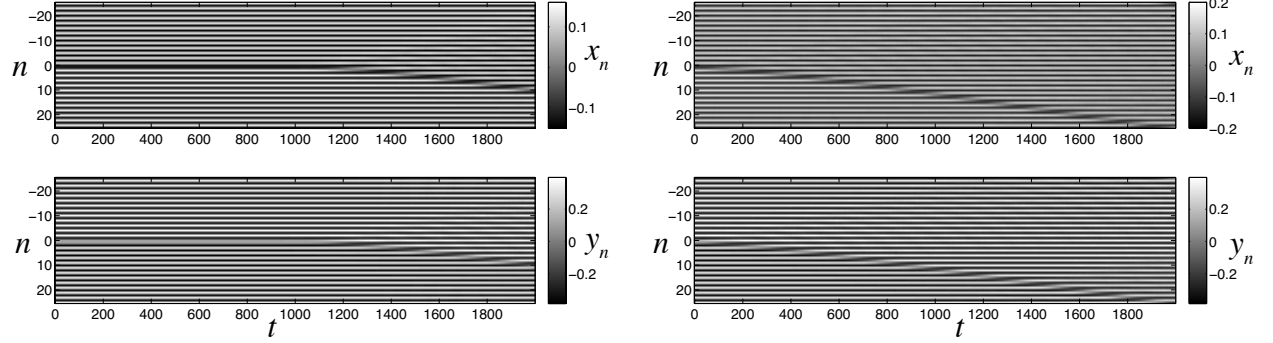


Figure 13: Left panel: contour plot of the time evolution of the bond-centered solution for $\omega_b = 2.05$. The color bar corresponds to the magnitude of the strain x_n (top) and y_n (bottom). Right panel: same simulation as in the left panel but with the perturbed dark breather as the initial condition. Here $\kappa = 1$ and $\rho = 1/3$.

increased the same phenomenology (dismantling of the breather and chaotic evolution) is also taking place for the bond-centered breathers, as shown in Fig. 14.

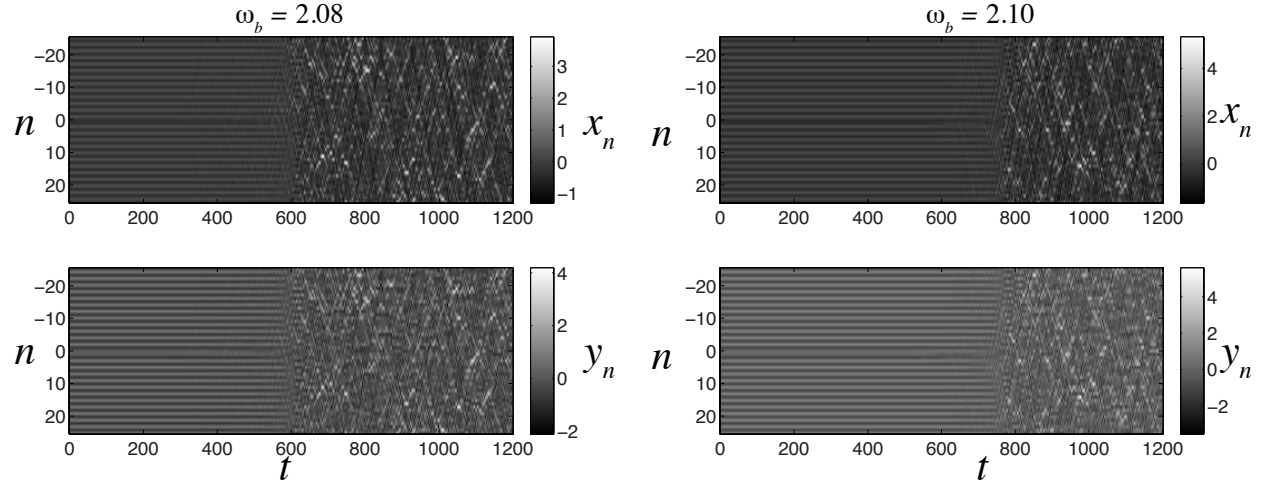


Figure 14: Left panel: contour plot of the time evolution of the bond-centered solution for $\omega_b = 2.08$. The color bar corresponds to the magnitude of the strain x_n (top) and y_n (bottom). Right panel: same simulation as in the left panel but at frequency $\omega_b = 2.10$. Here $\kappa = 1$ and $\rho = 1/3$.

The large arc seen in the middle of the Floquet multiplier diagram of the bond-centered breather solutions (the top left plot in Fig. 10) corresponds to the *period-doubling bifurcation*. As the frequency approaches $\omega_b \approx 2.063$, two complex conjugate eigenvalues collide on the real axis at -1 . Two real eigenvalues then form and move in opposite directions as ω_b increases. After the difference between the real eigenvalues reaches a maximum value, they

start moving toward each other and collide at $\omega_b \approx 2.096$. Breathers with double the period (half the frequency) of the ones on the main branch exist between these two frequencies.

To explore the numerically exact period-doubling orbits, we constructed an initial seed by slightly perturbing the dark breather solution at the bifurcation point along the direction of eigenvector associated with the eigenvalue -1 . As shown in Fig. 15, the eigenvector is spatially localized at the middle of the chain. As a consequence, the initial seed only differs from the previous dark breather solution in the middle part of the chain. Sample profiles of

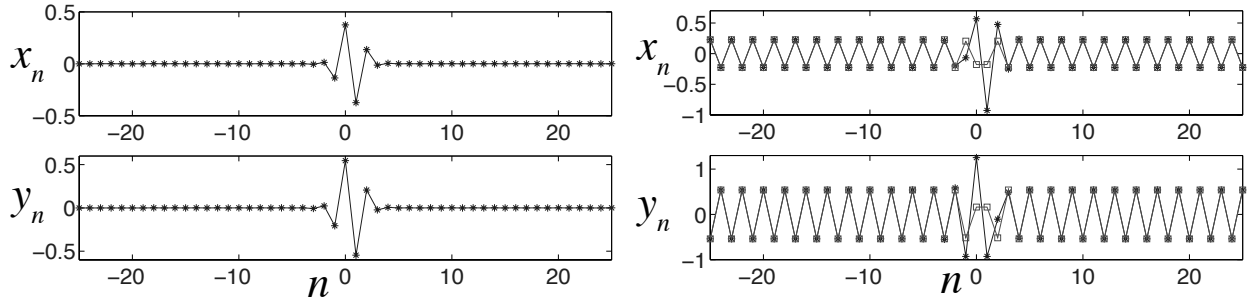


Figure 15: Left panel: the eigenvector associated with the eigenvalue -1 . Right panel: numerically exact dark breather solution of frequency $\omega_b = 1.032$ (connected squares) and the initial seed (connected stars) obtained by perturbing numerically exact dark breather solution of frequency $\omega_b = 2.063$.

period-doubling dark breather solution at $\omega_b = 1.032$ are shown in the top of Fig. 16. To check that these solutions differ from the main branch, we integrated the solution for both the full period $T_b = 2\pi/\omega_b$ and its half $T_b/2$ and verified that the period of the obtained new solution is doubled compared with the previously obtained dark breathers. The continuation method is used to obtain all the period-doubling dark breather solutions for different frequencies. Note that the continuation stops at $\omega_b \approx 1.051$ and also cannot proceed for ω_b below 1.032, which agrees with the (doubled) frequency range of the large arc in the top left plot of Fig. 10. All of these solutions exhibit both real and oscillatory instabilities (see the bottom plots of Fig. 16).

We now investigate the effect of mass ratio ρ on the system by repeating the same experiment for relatively large and small values ρ . Recall that the linear frequency $\omega = \sqrt{\kappa + \kappa/\rho}$ decreases and approaches $\sqrt{\kappa}$ as ρ increases. In what follows, we start the continuation at frequency $\omega_b = \omega + 0.01$ to make sure that the amplitude of the initial seed (89) is small. We first test the case when $\rho = 3$ with linear frequency given by $\omega = 1.1547$. Sample profiles of bond-centered and site-centered dark breather solutions at the frequency $\omega_b = \omega + 0.1 = 1.2547$ and their space-time evolution diagrams are shown in Fig. 17. We observe the bond-centered solution starts to move in form of a traveling dark breather after the integration for a sufficiently long time, while the site-centered solution persists for a longer time in the simulation and hence can be considered to be long-lived. The dynamic behavior of both solutions is consistent with their numerically computed Floquet spectrum shown in the right of Fig. 18. Moreover, the diagrams of Floquet multipliers' moduli in the right panel of Fig. 18 suggest that the bond-centered solutions exhibit only real instability for a wide range of frequencies $[\omega + 0.001, \omega + 0.2]$, while the site-centered dark breathers have just marginal oscillatory instability.

Next, we repeat the simulation with $\rho = 10$ and $\omega = 1.0488$. Note that the amplitude of

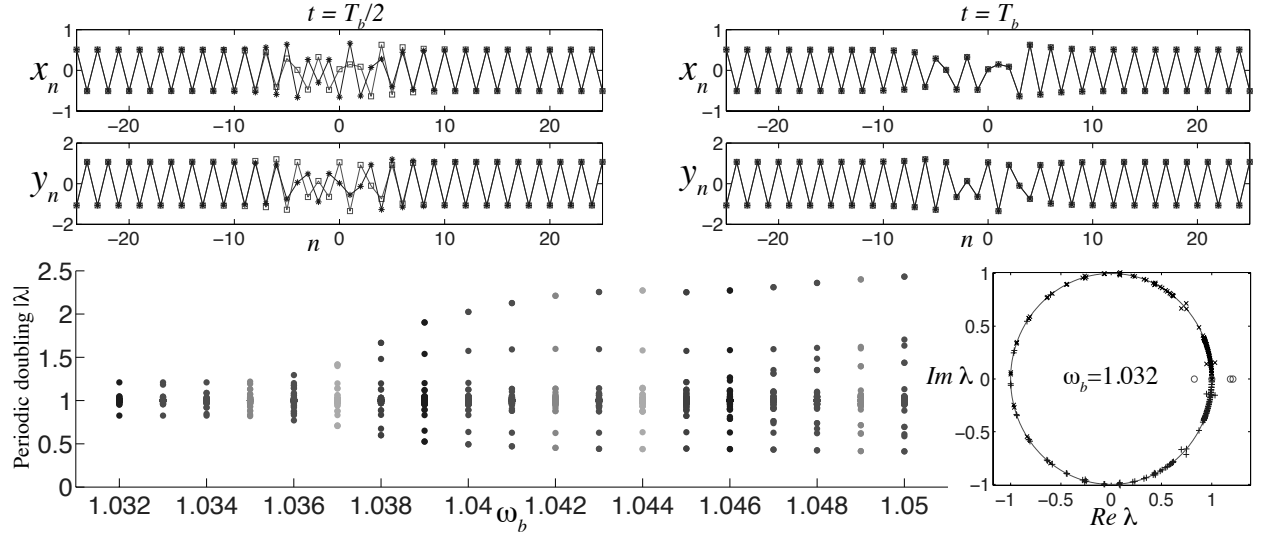


Figure 16: Top panel: comparison of the numerically exact double-period solution at $\omega_b = 1.032$ (connected squares) and the result of its integration (connected stars) at $t = T_b/2$ and $t = T_b$. Bottom left: moduli of Floquet multipliers versus frequency ω_b for the period-doubling solutions. The Floquet multipliers for $\omega_b = 1.032$ in the complex plane are shown in the right plot. Here $\kappa = 1$ and $\rho = 1/3$.

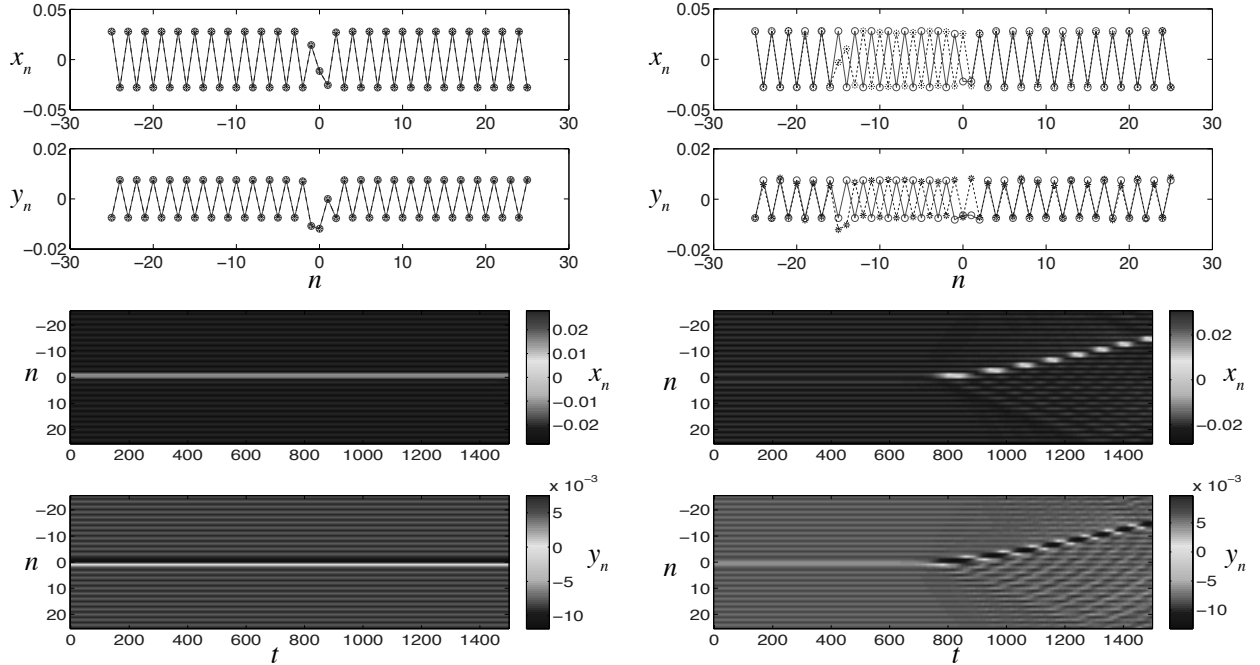


Figure 17: Top panel: sample profiles (circles) of site-centered (left) and bond-centered (right) dark breathers at the frequency $\omega_b = 1.2547$. Stars connected by dashed lines represent strain profiles after the integration over $299T_b \approx 1500$. Note that the site-centered solution has relative error $E_b(1500) = 9.21 \times 10^{-5}$. Bottom panel: space-time evolution diagrams for site-centered (left) and bond-centered (right) solutions. Here $\kappa = 1$ and $\rho = 3$.

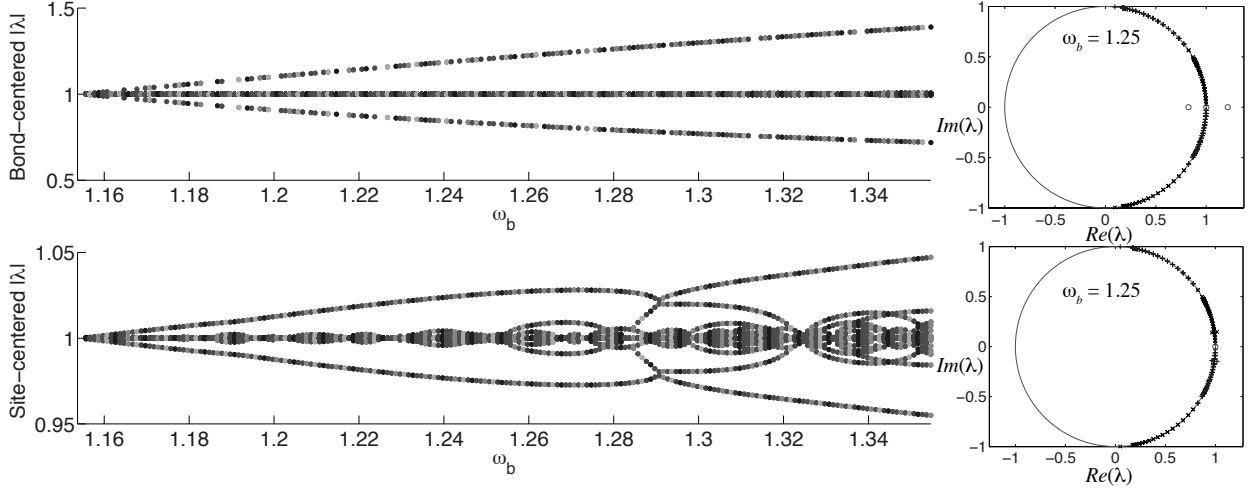


Figure 18: Left panel: moduli of Floquet multipliers versus frequency ω_b for the bond-centered (top) and site-centered (bottom) types. Right panel: Floquet multipliers of dark breather solutions of frequency $\omega_b = 1.2547$ in the complex plane. Here $\kappa = 1$ and $\rho = 3$.

dark breather solution at frequency $\omega_b = \omega + 0.01$ is close to 1.6×10^{-4} . As shown in Fig. 19, the pattern of Floquet multipliers moduli is very similar to the $\rho = 3$ case for breather frequencies close to ω . However, as ω_b becomes larger, we observed significant oscillatory instability of both the bond-centered and site-centered solutions. Note that the distribution of Floquet multipliers at large mass ratios (for example, $\rho = 3, 10$) is completely different than that at smaller ones (such as $\rho = 1/3$), given the same magnitude of frequency difference $\omega_b - \omega$.

We now fix the breather frequency ω_b and perform the continuation in the mass ratio ρ . The results of numerical continuation are shown in Fig. 20. At a given breather frequency, the real instability is only exhibited by solutions of the bond-centered type, and its significance is gradually increasing as mass ratio becomes larger. In contrast, the site-centered solutions have marginal oscillatory instability and persist for a long time. Moreover, the lifetime of those solutions decreases as the mass ratio increases. At a larger frequency like $\omega_b = 2.05$ and small mass ratio, the emergence of many unstable quartets suggests that both bond-centered and site-centered solutions share strong modulational instability of the background, which leads to a chaotic evolution of both solutions after a short time of integration.

8 Concluding remarks

In this work, we studied nonlinear waves in a resonant granular material modeled by a Hertzian chain of identical particles with a secondary mass attached to each bead in the chain by a linear spring. Following the approach developed in [15] for a limiting case of the present model, we derived generalized modulation equations of DpS type. We showed that for suitable initial data and large enough mass ratio, these equations reduce to the DpS equation derived in [15] and rigorously justified the equation in this limit on the long time scales. We then used the DpS equations to investigate the time-periodic traveling wave of

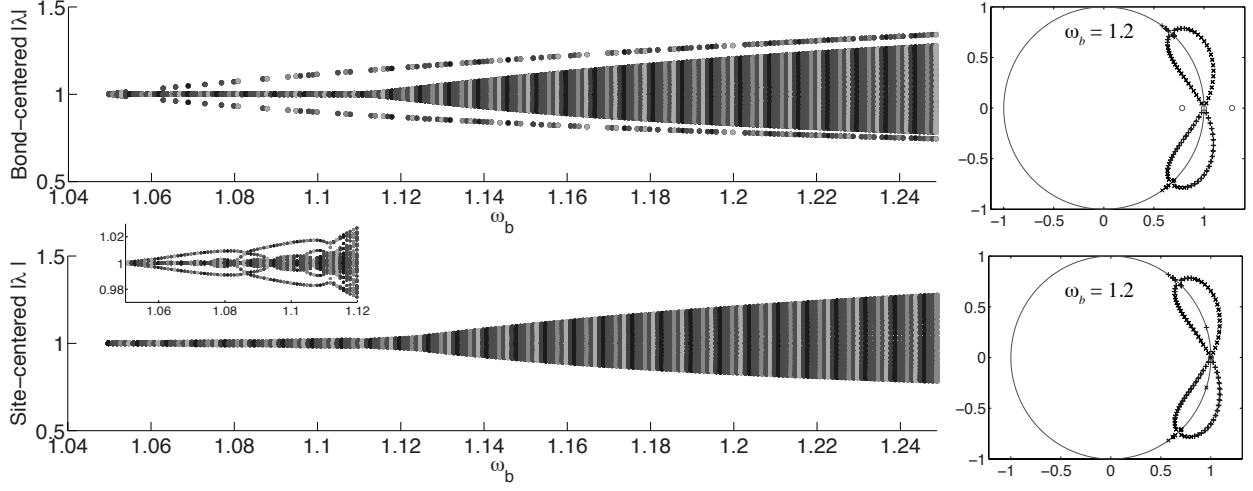


Figure 19: Left panel: moduli of Floquet multipliers versus frequency ω_b for the bond-centered (top) and site-centered (bottom) types. Right panel: Floquet spectrum of dark breather solutions of frequency $\omega_b = 1.20$ in the complex plane. The inset represents the zoom-in of moduli of Floquet multipliers for the site-centered solution at the frequencies $\omega_b \in [w + 0.001, w + 0.07]$. Here $\kappa = 1$ and $\rho = 10$.

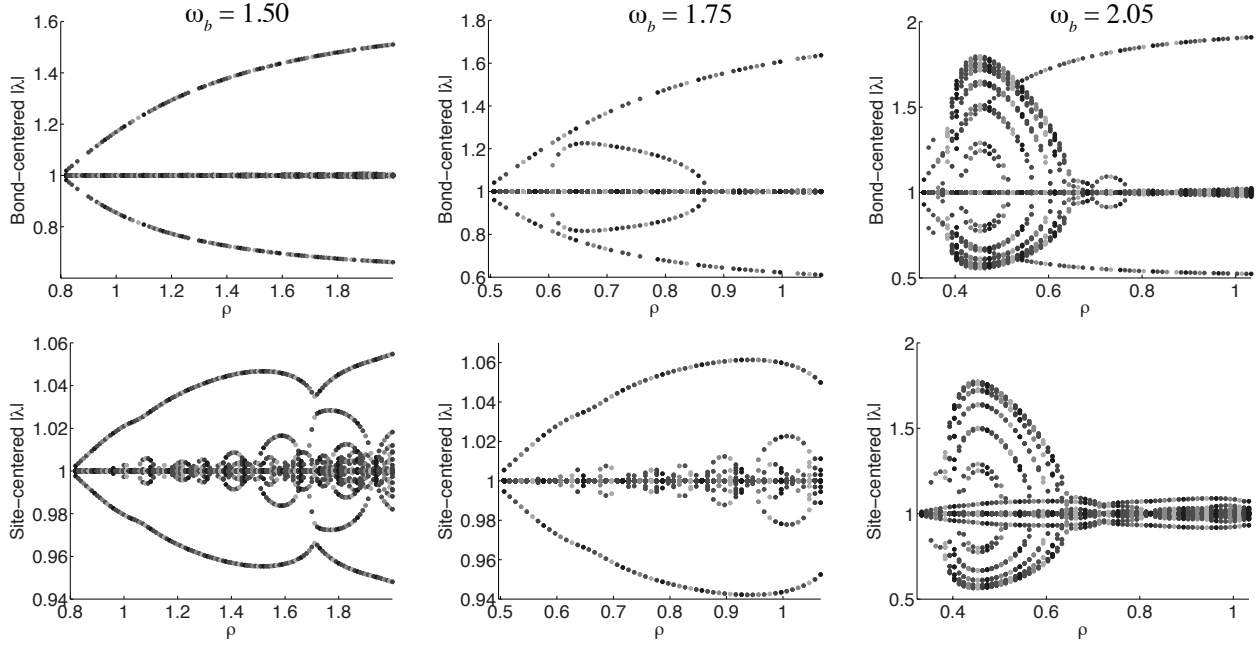


Figure 20: Moduli of Floquet multipliers versus mass ratio ρ for the bond-centered (top) and site-centered (bottom) type. The tested frequencies of the dark breather are $\omega_b = 1.50, 1.75$ and 2.05 . Here $\kappa = 1$.

the system at finite mass ratio. We showed numerically that these equations can successfully capture the dynamics of small-amplitude periodic traveling waves.

Turning our attention to the breather-type solutions, we proved non-existence of nontrivial bright breathers at finite mass ratio. However, we also showed that at sufficiently large mass ratio and suitable initial data, the problem has long-lived bright breather solutions.

The generalized DpS equations were also used to construct well-prepared initial conditions for the numerical computation of dark breather solutions. A continuation procedure based on a Newton-type fixed point method and initiated by the approximate dark breather solutions obtained from the DpS equations was utilized to compute numerically exact dark breathers for a wide range of frequencies and at different mass ratios. The stability and the bifurcation structure of the numerically exact dark breathers of both bond-centered and site-centered types were examined. Our numerical results strongly suggest that the bond-centered solutions exhibit real instability that may give rise to steady propagation of a dark breather after large enough time. In addition, period-doubling bifurcations of these solutions were identified at small mass ratios. The site-centered solutions, in contrast to the bond-centered ones, appeared to exhibit only oscillatory instability, which is much weaker than the real instability of the bond-centered breathers for a range of breather frequencies that are close enough to the natural frequency of the system, i.e., the frequency of out-of-phase motion within each unit cell of the chain involving the particle and the secondary mass. As a consequence, these low-frequency site-centered solutions persisted for a long time in the numerical simulation, and thus the effect of oscillatory instability is quite weak. However, we also provided case examples of their (long-time) instabilities that led to their complete destruction and ensuing apparently chaotic dynamics within the lattice. We showed that the distribution of Floquet multipliers and hence stability of the dark breather solutions are significantly affected by the mass ratio and breather frequency.

A challenge left for the future work is to rigorously prove the existence of small-amplitude exact periodic traveling wave and dark breather solutions of system (2) using the approximate solutions obtained from the generalized DpS equations. Another intriguing aspect to further consider involves the mobility of the dark breathers, and its association with the dynamical instability of the states, as well as possibly with the famous Peierls-Nabarro barrier associated with the energy difference between bond- and site-centered solutions, i.e., the energy barrier that needs to be “overcome” in order to have mobility of the dark breathers. Equally important and relevant would be an effort to analytically understand the modulational stability properties of the lattice, perhaps at the DpS level and compare them with corresponding systematic numerical computations. On the experimental side, it will be interesting to investigate whether we can generate dark breathers by exciting the both ends of a finite chain in a way similar to [7]. Additionally, exciting small amplitude traveling waves through boundary excitations, e.g. in the woodpile chain of [22] and observing experimentally their evolution through lased Doppler vibrometry would also be particularly relevant.

Acknowledgements. G.J. acknowledges financial support from the Rhône-Alpes Complex Systems Institute (IXXI). The work of L.L. and A.V. was partially supported by the US NSF grant DMS-1007908. P.G.K. gratefully acknowledges the support of US AFOSR through grant FA9550-12-1-0332. P.G.K.’s work at Los Alamos is supported in part by the US Department of Energy.

References

- [1] V. F. Nesterenko. *Dynamics of Heterogeneous Materials*. Springer, New York, 2001.
- [2] Surajit Sen, Jongbae Hong, Jonghun Bang, Edgar Avalos, and Robert Doney. Solitary waves in the granular chain. *Phys. Rep.*, 462(2):21 – 66, 2008.
- [3] C. Coste, E. Falcon, and S. Fauve. Solitary waves in a chain of beads under Hertz contact. *Phys. Rev. E*, 56(5):6104, 1997.
- [4] E. B. Herbold and V. F. Nesterenko. Shock wave structure in a strongly nonlinear lattice with viscous dissipation. *Phys. Rev. E*, 75:021304, Feb 2007.
- [5] Alain Molinari and Chiara Daraio. Stationary shocks in periodic highly nonlinear granular chains. *Phys. Rev. E*, 80:056602, Nov 2009.
- [6] N. Boechler, G. Theocharis, S. Job, P. G. Kevrekidis, Mason A. Porter, and C. Daraio. Discrete breathers in one-dimensional diatomic granular crystals. *Phys. Rev. Lett.*, 104(244302), 2010.
- [7] C. Chong, F. Li, J. Yang, M. O. Williams, I. G. Kevrekidis, P. G. Kevrekidis, and C. Daraio. Damped-driven granular chains: An ideal playground for dark breathers and multibreathers. *Phys. Rev. E*, 89:032924, Mar 2014.
- [8] M. Arif Hasan, Shihuh Cho, Kevin Remick, Alexander F. Vakakis, D. Michael McFarland, and Waltraud M. Kriven. Experimental study of nonlinear acoustic bands and propagating breathers in ordered granular media embedded in matrix. *Granul. Matter*, 17:49–72, 2015.
- [9] Serge Aubry. Breathers in nonlinear lattices: Existence, linear stability and quantization. *Physica D*, 103(14):201 – 250, 1997.
- [10] S. Flach and A. Gorbach. Discrete breathers: advances in theory and applications. *Phys. Rep.*, 467:1–116, 2008.
- [11] G. Hoogeboom and P. G. Kevrekidis. Breathers in periodic granular chain with multiple band gaps. *Phys. Rev. E*, 86(061305), 2012.
- [12] G. Theocharis, N. Boechler, S. Job, P. G. Kevrekidis, M. A. Porter, and C. Daraio. Intrinsic energy localization through discrete gap breathers in one-dimensional diatomic granular crystal. *Phys. Rev. E*, 82(056604), 2010.
- [13] G. Theocharis, M. Kavousanakis, P. G. Kevrekidis, C. Daraio, M. A. Porter, and I. G. Kevrekidis. Localized breathing modes in granular crystals with defects. *Phys. Rev. E*, 80(066601), 2009.
- [14] Stéphane Job, Francisco Santibanez, Franco Tapia, and Francisco Melo. Wave localization in strongly nonlinear Hertzian chains with mass defect. *Phys. Rev. E*, 80:025602, Aug 2009.

- [15] G. James. Nonlinear waves in Newton’s cradle and the discrete p-Schrödinger equation. *Math. Mod. Meth. Appl. Sci.*, 21(11):2335–2377, 2011.
- [16] G. James, P. G. Kevrekidis, and J. Cuevas. Breathers in oscillator chains with Hertzian interactions. *Physica D*, 251:39–59, 2013.
- [17] B. Bidégaray-Fesquet, E. Dumas, and G. James. From Newton’s cradle to the discrete p-Schrödinger equation. *SIAM J. Math. Anal.*, 45:3404–3430, 2013.
- [18] C. Chong, P. G. Kevrekidis, G. Theocharis, and Chiara Daraio. Dark breathers in granular crystals. *Phys. Rev. E*, 87(042202), 2013.
- [19] L. Bonanomi, G. Theocharis, and C. Daraio. Wave propagation in granular chains with local resonances. *Phys. Rev. E*, 91(033208), 2015.
- [20] G. Gantzounis, M. Serra-Garcia, K. Homma, J. M. Mendoza, and C. Daraio. Granular metamaterials for vibration mitigation. *J. Appl. Phys.*, 114(093514), 2013.
- [21] P. G. Kevrekidis, A. Vainchtein, M. Serra Garcia, and C. Daraio. Interaction of traveling waves with mass-with-mass defects within a Hertzian chain. *Phys. Rev. E*, 87(042911), 2013.
- [22] E. Kim and J. Yang. Wave propagation in single column woodpile phononic crystal: Formation of tunable band gaps. *J. Mech. Phys. Solids*, 71:33–45, 2014.
- [23] E. Kim, F. Li, C. Chong, G. Theocharis, J. Yang, and P.G. Kevrekidis. Highly nonlinear wave propagation in elastic woodpile periodic structures. *Phys. Rev. Lett.*, 114(118002), 2015.
- [24] H. Xu, P.G. Kevrekidis, and A. Stefanov. Traveling Waves and their Tails in Locally Resonant Granular Systems. *J. Phys. A: Math. Theor.*, 48(195204), 2015.
- [25] G. James and Y. Starosvetsky. Breather solutions of the discrete p -Schrödinger equation. In R. Carretero-Gonzalez, J. Guevas-Maraver, D. Frantzeskakis, N. Karachalios, P. Kevrekidis, and F. Palmero-Acebedo, editors, *Localized Excitations in Nonlinear Complex Systems*, volume 7 of *Nonlinear Systems and Complexity*, pages 77–115. Springer, 2014.
- [26] H. Yoshida, C. Chong, E. Charalampidis, P.G. Kevrekidis, and J. Yang. Formation of rarefaction waves in origami-based metamaterials. *arXiv*, page 1505.03752, 2015.
- [27] Alexandre Rosas, Aldo H. Romero, Vitali F. Nesterenko, and Katja Lindenberg. Observation of two-wave structure in strongly nonlinear dissipative granular chains. *Phys. Rev. Lett.*, 98:164301, Apr 2007.
- [28] R. Carretero-González, D. Khatri, Mason A. Porter, P. G. Kevrekidis, and C. Daraio. Dissipative solitary waves in granular crystals. *Phys. Rev. Lett.*, 102:024102, Jan 2009.
- [29] S. Hutzler, G. Delaney, D. Weaire, and F. MacLeod. Rocking Newton’s cradle. *Am. J. Phys.*, 72(12):1508–1516, 2004.

- [30] T. Cretegny and S. Aubry. Spatially inhomogeneous time-periodic propagating waves in anharmonic systems. *Phys. Rev. B*, 55(18), 1997.
- [31] G. James. Periodic travelling waves and compactons in granular chains. *J. Nonlinear Sci.*, 22:813–848, 2012.